



Chair of Ferrous Metallurgy

Master's Thesis



IoT for clogging and refractory wear
detection

Patricia Polatschek, BSc

July 2022



Frau **Patricia POLATSCHEK** wird vom Lehrstuhl für Eisen- und Stahlmetallurgie folgendes Masterarbeitsthema **S744** gestellt:

Internet of Things for clogging and refractory wear detection

Clogging is still an ongoing issue and limits productivity during continuous casting, whereas wear, e.g., in the ladle shroud can lead to health & safety issues due to potential breakages. Examples for the current state of the art clogging detection contain mould level fluctuations as well as stopper rod movement measurements. To minimize the risk of ladle shroud breakages, a standardized maximum amount of shroud uses can be one solution, but with subsequent drawback of using the complete ladle shroud lifetime potential.

The theoretical part of this Master Thesis should evaluate typically used refractory materials, fundamentals about clogging and refractory wear mechanisms, as well as current detection methods regarding clogging and refractory wear. The practical part deals with a lab trial setup, aiming on the investigation of contactless measurement methods regarding temperature changes on isostatically pressed refractory material (Ladle shrouds, Monotubes, Submerged Entry Nozzles).

Content:

- Literature survey
 - Refractory materials for continuous casting purposes
 - Casting problems (clogging and wear)
 - Temperature measurement
- Experimental work
 - Laboratory trials with a special experimental test procedure
 - Temperature measurement using different methods
- Discussion, Comparison and Summary of Results

Industry Partner:



Leoben, October 2021

Assoz. Prof. Dr. Susanne Michelic

Kurzfassung

Obwohl das Stranggießen heutzutage das am meisten verwendete Verfahren für das Vergießen von Stahl ist, wird der Hersteller nach wie vor mit mehreren Herausforderungen konfrontiert. Diese können unter anderem Produktfehler wie Risse oder nichtmetallische Einschlüsse sowie betriebliche Probleme wie Durchbrüche der Strangschale oder Clogging während des Gießens sein.

Um Clogging und feuerfesten Verschleiß frühzeitig zu erkennen und damit schwerwiegendere Probleme wie zuvor genannte Durchbrüche zu vermeiden, wurde in dieser Arbeit eine neue Methode zur Detektion dieser beiden Probleme getestet. Das Ziel dieser Arbeit ist es, die Erkennung von Clogging und feuerfestem Verschleiß mithilfe der berührungslosen Temperaturmessung zu evaluieren. Hierfür wurde ein spezieller Laborversuchsaufbau entwickelt, um Messungen mit verschiedenen berührungslosen Temperaturmessmethoden gleichzeitig durchführen zu können. Dafür wurden eine Infrarot-Kamera, ein Pyrometer und das BST (Broadband Spectral Thermometer) verwendet. Des Weiteren wurden Thermoelemente als Referenz für die kontaktlosen Messungen verwendet. Um die geeignetste Methode zum Nachweis von Ansatzbildung und feuerfesten Verschleiß zu finden, wurden die verschiedenen Methoden hinsichtlich der Endtemperaturdifferenz und der Aufheizgeschwindigkeit der verschiedenen Proben verglichen.

Grundsätzlich ist die Detektion von Clogging und Verschleiß in einem Labormaßstab möglich. Das gilt sowohl für die Betrachtung der Endtemperaturdifferenz als auch für die Aufheizgeschwindigkeit. Dabei zeigte das Pyrometer die besten Ergebnisse.

Abstract

Although continuous casting is the dominating casting process nowadays, the operators still face several challenges. These can be product defects and operational difficulties, like different cracks, non-metallic inclusions, breakouts or the appearance of clogging, respectively.

To detect clogging and refractory wear at an early stage and thus avoid more severe problems, a new approach was tested in this work. The main objective was to answer whether the detection of clogging and refractory wear can be measured using contactless temperature measurement. Thus, developing a laboratory trial set-up was necessary to conduct measurements with various contactless temperature measurement methods, e.g., Infrared Camera, Pyrometer, and Broadband Spectral Thermometer. Furthermore, thermocouples were used as a reference. The different methods were compared concerning the end temperature difference and the heating rate of the different samples to find the most sufficient method to detect clogging and refractory wear.

It was found that the detection of both, clogging and wear, is possible in a laboratory scale. This is true if the end temperatures are taken into consideration as well as in case of the comparison of heating rates. Whereat, the pyrometer showed the best results.



EIDESSTÄTLICHE ERKLÄRUNG

Ich erkläre an Eides statt, dass ich diese Arbeit selbständig verfasst, andere als die angegebenen Quellen und Hilfsmittel nicht benutzt, und mich auch sonst keiner unerlaubten Hilfsmittel bedient habe.

Ich erkläre, dass ich die Richtlinien des Senats der Montanuniversität Leoben zu "Gute wissenschaftliche Praxis" gelesen, verstanden und befolgt habe.

Weiters erkläre ich, dass die elektronische und gedruckte Version der eingereichten wissenschaftlichen Abschlussarbeit formal und inhaltlich identisch sind.

Datum 04.07.2022

Patricia Polatschek

Unterschrift Verfasser/in
Patricia Polatschek

Table of Contents

Kurzfassung	I
Abstract.....	II
Declaration on honour	III
Table of Contents.....	IV
Acronyms.....	VII
List of figures	VIII
List of tables	XI
Glossary.....	XIII
1 Introduction.....	1
2 Refractory products for the continuous casting of steel	3
2.1 Types.....	4
2.1.1 Ladle shroud	4
2.1.2 Submerged entry nozzle.....	4
2.2 Material and shape concept.....	5
2.3 Wear mechanisms	6
2.4 State-of-the-art in wear detection.....	9
2.5 Countermeasures	10
3 Clogging	12
3.1 Clogging mechanisms	13
3.1.1 Transport of particles to a boundary layer and agglomeration of these	13

3.1.2	Build-up of solidified steel.....	14
3.1.3	Aspiration of air into the casting nozzle.....	14
3.1.4	Build-up of reaction products.....	15
3.2	State-of-the-art in clogging detection	15
3.2.1	Mould level fluctuations	15
3.2.2	Argon back pressure	16
3.2.3	Stopper rod movement or slide gate position.....	17
3.3	Countermeasures	18
3.3.1	Production of steel with higher cleanliness	18
3.3.2	Argon purging within the casting channel.....	19
3.3.3	Modification of inclusions via calcium treatment	20
3.3.4	Geometrical modifications of the nozzle.....	20
3.3.5	Modification of the nozzle material	21
4	Overview on temperature measurement.....	22
4.1	The principle of radiation thermometers.....	22
4.2	Pyrometer.....	25
4.3	BST (broadband spectral thermometer).....	27
4.4	Infrared camera	28
4.5	Thermocouples.....	30
4.6	Summary of temperature measurement methods	31
5	Experimental	33
5.1	Experimental set-up.....	33
5.2	Sample design and instrumentation.....	35
5.3	Test procedure	36
6	Results and discussion.....	38
6.1	Physical sample analysis	38
6.2	Temperature profiles.....	42
6.2.1	Infrared camera (FLIR).....	42
6.2.2	Pyrometer	46
6.2.3	BST	48
6.2.4	Thermocouples.....	49
6.3	Comparison	51
6.3.1	Wear	52
6.3.2	Clogging.....	53

6.3.3	Pyrometer	55
7	Summary and outlook	58
	List of References	61
A.	Physical sample analysis	A-1
B.	Temperature profiles	B-1
B.1	Infrared Camera.....	B-2
B.2	Pyrometer	B-3
B.3	Thermocouples.....	B-5

Acronyms

AES	alkaline earth silicate
BST	broadband spectral thermometer
CWTD	continuous wear testing device
EMF	electromotive force
FPA	focal plane array
IR	infrared
IRT	infrared thermography
ISO material	isostatically pressed material
LS	ladle shroud
MT	monotube
NMI	non-metallic inclusion
SEN	submerged entry nozzle
SES	submerged entry shroud

List of figures

- Figure 1-1:** Build-up of clogging material a) at the tundish slide gate, b) on the upper part of a submerged entry nozzle, and c) in the bore and the area of the exit ports of a SEN. [4] 1
- Figure 2-1:** Schematic drawings of isostatically pressed refractory parts for the continuous casting of steel, including the most typical materials of these products. [2]..... 6
- Figure 2-2:** Schematic drawing of a submerged entry nozzle including typical wear mechanisms in different areas. Redrawn after [1]..... 8
- Figure 2-3:** Exterior view (left picture) and furnace chamber of the Continuous Wear Testing Device at room temperature during measurement of an Al_2O_3 specimen (right picture). [10] 10
- Figure 2-4:** Characterization of the wear profile of submerged entry nozzles, left picture: typical wear profile of a used SEN, right picture: profile measurement result. [11]..... 10
- Figure 3-1:** Left picture: submerged entry nozzle after a short time of casting, right picture: clogged SEN. [19] 13
- Figure 3-2:** Mould level fluctuations due to clogging (left picture clogged SEN, right picture unclogged SEN) [14] 16
- Figure 3-3:** Pressure distribution in a standard tundish nozzle, which was calculated by a computational flow model. a) shaded contour plot, b) pressure profile along the centreline of the nozzle. [14]..... 17
- Figure 3-4:** Casting speed and stopper rod position in case of an unclogged SEN (upper picture) and a clogged SEN (lower picture) [26] 18
- Figure 3-5:** Two different purging plug types, (a) hybrid plug, (b) slot plug. [27] 19

Figure 3-6: Modification route of alumina inclusions modified by calcium. [29].....	20
Figure 4-1: Electromagnetic spectrum including the used range of the infrared area. [46]23	
Figure 4-2: Electromagnetic radiation of a black body over the wavelength for different temperatures. [40]	24
Figure 4-3: Specific electromagnetic radiation at different emissivity for a black body, a grey body and a non-grey body. [46]	24
Figure 4-4: Measurement spectrum of a broadband single colour pyrometer. Red area shows the wavelength range which is measured. [58]	26
Figure 4-5: Measurement spectrum of a narrow-bandwidth dual wavelength pyrometer. Red lines show the wavelengths, at which the intensity was measured. [58]	27
Figure 4-6: Measurement spectrum of the BST (upper picture) as well as the calculated/fitted black body curve at 1900 K. [58].....	28
Figure 4-7: Functional principle of scanning cameras (left side) and FPA cameras (right side). Redrawn after [61]	29
Figure 4-8: Schematic drawing of the functional principle of a thermal detector (left side) and a quantum detector (right side). Redrawn after [40].....	30
Figure 5-1: Schematic of the experimental set-up for the laboratory trials. On the left side the intersection of the furnace is shown, on the right sight the front view of the refractory frame including the sample and the drilled hole for the argon supply can be seen.....	34
Figure 5-2: Experimental set-up for the laboratory trials.....	34
Figure 5-3: Sample design and dimensions. Clogging (“C”) refers to a clogged submerged entry nozzle, Insulation (“I”) illustrates a SEN without clogging, Original (“O”) represents an original ladle shroud without wear, and Wear (“W”) should indicate wear in case of a ladle shroud.....	35
Figure 5-4: One sample of “W” with insulating wool on three sides, ready for laboratory trial.	36
Figure 6-1: Hot sample of case “C” directly after the laboratory trial with detached clogging layer besides (left picture). Hot face of the sample after cooling without the clogging layer (right picture).	41
Figure 6-2: Details of the cut sample of “I”. On the left side the cold face is shown and on the right sight the hot face can be seen. In addition, to illustrate the difference in thickness, an area of the decarbonized layer is marked with red areas.....	41

Figure 6-3: Left picture: temperature curves for each sample of “C”, right picture: mean temperature curve including standard deviation of “C”, obtained by IR camera	43
Figure 6-4: Summary of the mean temperature curves of all four cases, obtained by IR camera.....	45
Figure 6-5: Summary of the mean temperature curves of all four cases, obtained by pyrometer.....	47
Figure 6-6: Results of the measurement with the BST.....	48
Figure 6-7: Broken tip of the thermocouple in a sample of “I”.....	49
Figure 6-8: Summary of the mean temperature curves of all four cases, obtained by thermocouples.....	51
Figure 6-9: Upper diagram: more detailed diagram of the mean temperature curves of all four cases by measurement with the pyrometer. Lower diagram: detailed section of the starting points of the mean temperature curves.	56
Figure B-1: Detailed diagram of the differences in the end temperatures of the mean temperature curves obtained by measurement with the pyrometer.....	B-5
Figure B-2: Mean temperature curves obtained by thermocouples placed in the middle of the sample.....	B-6
Figure B-3: Mean temperature curves obtained by thermocouples placed near the surface of the sample.....	B-6
Figure B-4: Detailed diagram of the differences in the end temperatures of the mean temperature curves obtained by measurement with thermocouples.	B-8

List of tables

Table 2-1: Classification of refractory materials based on their chemical reaction behaviour. [2]	3
Table 2-2: Overview about Al ₂ O ₃ -C refractory material. [2].....	5
Table 2-3: Overview about wear mechanisms of refractory tubes. [1].....	7
Table 4-1: Evaluation of temperature measurement methods.	32
Table 5-1: Key parameters of the experimental set-up.	35
Table 5-2: Procedure of the laboratory tests.....	37
Table 6-1: Overview of the samples before the laboratory trials.	39
Table 6-2: Overview of the samples after the laboratory trials.	40
Table 6-3: Example of thermographs at the start and end of the by measurement with the infrared camera FLIR A615.	42
Table 6-4: Mean temperature curves of all four cases including standard deviation, obtained by the infrared camera FLIR A615.....	44
Table 6-5: Mean temperature curves of all four cases including standard deviation, obtained by the pyrometer Metis M3.	46
Table 6-6: Mean temperature curves of all four cases including standard deviation, obtained by the surface thermocouples, type N.	50
Table 6-7: Calculated heating rate (slope of a fitted straight line) for “O” and “W” on the mean temperature curves obtained by measurement with IR camera and thermocouples. ..	53

Table 6-8: Calculated heating rate (slope of a fitted straight line) for “C” and “I” on the mean temperature curves obtained by measurement with infrared camera and thermocouples.....	54
Table 7-1: Summary of the outcome of this thesis.....	59
Table A-1: Overview of the samples of “C” before and after the laboratory trials.....	A-1
Table A-2: Overview of the samples of “I” before and after the laboratory trials.	A-3
Table A-3: Overview of the samples of “O” before and after the laboratory trials.....	A-4
Table A-4: Overview of the samples of “W” before and after the laboratory trials.	A-6
Table B-1: Mean temperature curves of all four cases including standard deviation and the gradient ($\Delta T/\Delta t$), obtained by the infrared camera FLIR A615.	B-2
Table B-2: Individual temperature curves of each sample for all cases, obtained by measurement with the IR camera.....	B-3
Table B-3: Individual temperature curves of each sample for all cases, obtained by measurement with the pyrometer	B-4
Table B-4: Individual temperature curves of each sample for all cases, obtained by measurement with thermocouples placed on the surface.	B-7

Glossary

[1,2]	Alumina	Corundum, Al_2O_3
[1,2]	Chromia	Chromic oxide, Cr_2O_3
[1,2]	Magnesia Chromite	Chrome spinel, $\text{MgO} \cdot \text{Cr}_2\text{O}_3$
[1,2]	Calcia	Lime, Calcia, CaO
[1,2]	Doloma	Dolomite, $\text{CaCO}_3 \cdot \text{MgCO}_3$
[1,2]	Forsterite	$2\text{MgO} \cdot \text{SiO}_2$
[1,2]	Magnesia	Periclase, MgO
[1,2]	Silica	Cristobalite, SiO_2
[1,2]	Spinel	Magnesia Aluminate, $\text{MgO} \cdot \text{Al}_2\text{O}_3$
[1,2]	Zirconia	Baddeleyite, ZrO_2
[1,2]	Zircon	Zircon Silicate, $\text{ZrO}_2 \cdot \text{SiO}_2$
LS	Ladle shroud	Between ladle & tundish; pressed onto a collector nozzle using a LS manipulator
SEN	Submerged entry nozzle	directly mortared into the bottom of the tundish
SES	Submerged entry shroud	Between tundish & mould; pressed onto a collector nozzle using some manipulator (similar to ladle shroud)

MT	Monotube	Between tundish & mould; applied using an exchangeable nozzle system (compare to RHI Magnesita MNC-RSP system for open casting)
----	----------	---

1 Introduction

Nowadays the continuous casting process is primarily used for the casting of steel. Some problems come along with this process like product defects and operational difficulties. Product defects include cracks, various porosities, or non-metallic inclusions, whereas operational difficulties can include breakouts or clogging during the continuous casting of steel. The build-up of material can occur at various areas inside a continuous casting system. Some of them are shown in **Figure 1-1**. Additionally, clogging is also possible at the stopper nose. [3,4]

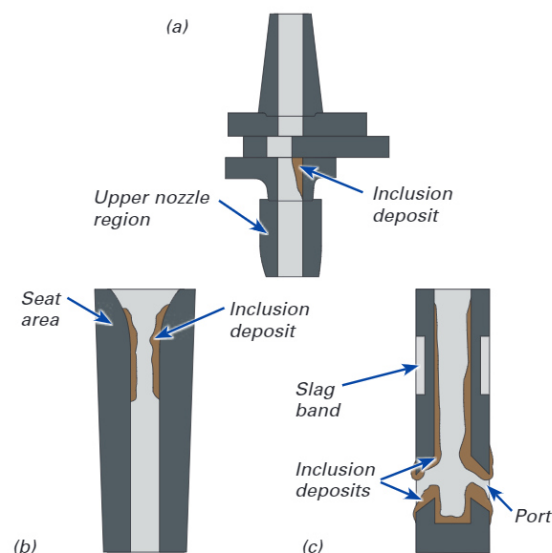


Figure 1-1: Build-up of clogging material a) at the tundish slide gate, b) on the upper part of a submerged entry nozzle, and c) in the bore and the area of the exit ports of a SEN. [4]

The early detection of problems as clogging or refractory wear can be essential to prevent more serious problems as for example breakouts. Thus, it should be clarified within this work if the detection of clogging and refractory wear using contactless temperature measurement is

feasible. Therefore, a literature study was conducted regarding refractory materials and types, clogging, as well as the principles of contactless temperature measurements and thermocouples. Afterwards, a laboratory trial set-up was developed to conduct temperature measurements with an infrared camera, a pyrometer, and a broadband spectral thermometer. Additionally, thermocouples were applied as a reference. The different contactless temperature measurement methods were compared, to find the most sufficient for the detection of clogging and refractory wear.

2 Refractory products for the continuous casting of steel

In this chapter a short overview about the refractory products for the continuous casting of steel is given. The functional products, more precisely refractory tubes, are explained in more detail regarding structure and wear mechanisms, as well as wear detection and typical countermeasures.

Refractory products are defined as non-metallic ceramic materials which have a refractoriness of ≥ 1500 °C. Refractory products are based on six raw materials or mixtures of these – SiO_2 , Al_2O_3 , MgO , CaO , Cr_2O_3 and ZrO_2 . Also, carbon is often added. These materials can be divided according to their chemical reaction behaviour into acidic, basic and neutral, also see **Table 2-1**. [2]

Table 2-1: Classification of refractory materials based on their chemical reaction behaviour. [2]

chemical reaction behaviour	reaction	refractory material
acidic	$\text{oxide} + \text{H}_2\text{O} \rightarrow \text{acid}$	silica, Al_2O_3 - SiO_2 -products, zircon silicate
basic	$\text{oxide} + \text{H}_2\text{O} \rightarrow \text{base (hydroxide)}$	products with magnesia and doloma base
almost neutral	reacts neither acidic nor basic	alumina, chromite, picrochromite, spinel, forsterite

2.1 Types

According to literature, there are four types of refractory products [2]:

- shaped products,
- unshaped products or monolithics,
- functional products, and
- heat-insulating products.

This master thesis focuses on functional products, more precise on isostatically pressed products for the continuous casting of steel. Among this group are ladle shrouds and submerged entry nozzles which will be described more detailed in the following subchapters. [2]

2.1.1 Ladle shroud

The ladle shroud is a pipe made of refractory material and is used to protect the molten metal stream which is transferred from the ladle to the tundish. Primarily, it should shield the molten metal from contact with ambient air. Thus, preventing reoxidation, slag entrapment and air-pickup, which can lead to formation of inclusions. The shrouding furthermore has been adapted by argon injection or gaskets to minimize air suction into the nozzle through cracks or joints between the shroud and the collector nozzle (CN). The reduction of temperature losses during casting is a further benefit using a ladle shroud. [2,5]

2.1.2 Submerged entry nozzle

Just like the ladle shroud, the submerged entry nozzle (SEN) is a tube made of refractory material. For the use in the continuous casting of steel the following characteristics of SENs are among others favourable [6–8]:

- stability in temperatures up to 1600 °C,
- low chemical reactivity of the refractory material with molten metal,
- erosion resistance, even at high flow rates, and
- low porosity.

A submerged entry nozzle is used to shroud the casting stream transferred from tundish to mould. Apart from protecting the molten metal from the contact with the ambient air, and thus

prevent re-oxidation, the SEN is also used to control the molten steel flow in the mould. In order to optimize this flow pattern different designs are used. [6–8]

2.2 Material and shape concept

For both, ladle shroud and submerged entry nozzle, in general the raw material concept is based on a mixture of alumina and graphite. Typically, the nozzles own a wall thickness of 35 – 50 mm. In **Table 2-2** an overview about the material concept as well as the production process is given. [1,5,8,9]

Table 2-2: Overview about $\text{Al}_2\text{O}_3\text{-C}$ refractory material. [2]

material	alumina-(silica)-graphite
raw material component	flake graphite, fused corundum, calcined alumina sometimes fused silica, sometimes antioxidants
primary binder	resin
shaping	isostatic pressing
thermal treatment	coking in reducing atmosphere at 800 to 1.000 °C
bond after thermal treatment	carbon
application	base material for continuous casting

The used $\text{Al}_2\text{O}_3\text{-C}$ material is a mixture of approximately 20 – 25 % graphite and approximately 70 – 75 % alumina. Furthermore, additions of 0 – 5 % zirconia and varying amounts of antioxidants (Al, Si, boron, etc.) to protect the carbon are possible. In **Figure 2-1** schematic drawings of isostatically pressed parts for the continuous casting of steel, including the most typical materials, are shown. Regarding SENs, an inner liner of various materials, like low silica or low carbon, as well as high free lime for example, is used in order to prevent or minimize clogging. Based on findings in operation and continuous product improvement, different material combinations are used today to withstand the given casting conditions in certain areas of the products like the stopper seat or stopper tip. Additionally, a slag line of different refractory material, which matches the present slag to reduce wear is used in case of the ladle shroud. A slag line of $\text{ZrO}_2\text{-C}$ is often applied in case of SEN. [1,5,8,9]

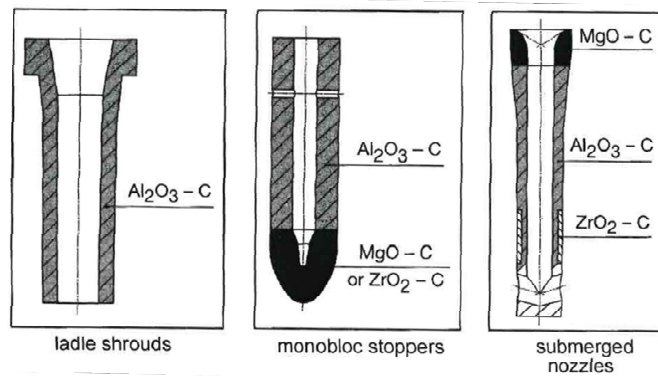


Figure 2-1: Schematic drawings of isostatically pressed refractory parts for the continuous casting of steel, including the most typical materials of these products. [2]

2.3 Wear mechanisms

The wear mechanisms of refractory tubes can be classified in three main mechanisms. These are as follows [1]:

- thermal,
- mechanical, and
- chemical.

Furthermore, also a combination of these three mechanisms is usually observed. As the various mechanisms take place in different locations of the ladle shroud, the combination effect is rather small. Contrary, in case of the submerged entry nozzles the combination of abrasion, corrosion, and thermal cycling leads to the usually low lifetime of 3 – 10 heats. In **Table 2-3** an overview about main wear mechanisms, sub mechanisms, and examples for ladle shrouds and submerged entry nozzles is given. [1]

Table 2-3: Overview about wear mechanisms of refractory tubes. [1]

main mechanism	sub mechanism	example
thermal	peak temperature (T)	Inside the ladle shroud or SEN, the temperature of the molten metal is reached. Only very high temperature resistant materials can withstand these temperatures.
	thermal shock (ΔT)	Due to the fact, that the ladle shroud typically is not preheated, thermal shock is a big problem. Also, during ladle change a significant thermal shock can possibly occur. In case of the submerged entry nozzles, this problem is not as big, due to preheating of the SEN before use. Since SENs are very sensitive regarding the cool down time they are rejected if not used directly after preheating. To increase the thermal conductivity and enhance the thermal shock resistance of refractory tubes, Carbon is added.
mechanical	impact	Usually, the impact on ladle shrouds or SENs is low and therefore it has only small influence on the wear. However, in case of the submerged nozzle flange cracks can occur from rough SEN changes, which can lead to air aspiration problems.
	abrasion	The quantity of abrasion depends on the throughput rate of the molten metal, as well as on the bore diameter. This applies for both, ladle shroud and submerged nozzles. Regarding SENs, it must be stated that a too large bore diameter leads to clogging because of a stagnant boundary layer due to low velocity, whereas a too small diameter results in a lower throughput. Furthermore, the abrasion in case of the SEN is highest on the sliding surfaces at the top, which can lead to steel fins and therefore to a failure during SEN change, causing a casting stop. Coming back to the ladle shroud, abrasion is also a problem on the outside caused by the molten metal bath and slag inside the tundish.
	applied stress	Applied stresses are not a key factor regarding wear, because other than in the holding mechanism, the tubes are able to expand or contract as needed.

main mechanism	sub mechanism	example
chemical	dissolution	Wear by dissolution on ladle shrouds is only a factor on the outside, more precisely in slag line area. In contrast, with focus on submerged entry nozzles, dissolution not only occurs on the outside but also on the inside of the nozzle. Dissolution of the refractory material in the inner nozzle can lead to build-up of clogging material (alumina and/or spinel).
	penetration	Low viscosity metals and/or slags or highly wetting metals/slugs can penetrate porous refractory. For ladle shrouds especially oxygen lancing of the top can create high wear due to penetration. In case of SENs the penetration usually is a problem on the outside of the tube, where rapid wear due to penetration is observed because of mould flux inside the continuous casting mould.

In **Figure 2-2** a schematic drawing of a submerged entry nozzle is shown. Furthermore, the typical wear mechanisms in various areas can be seen. [1]

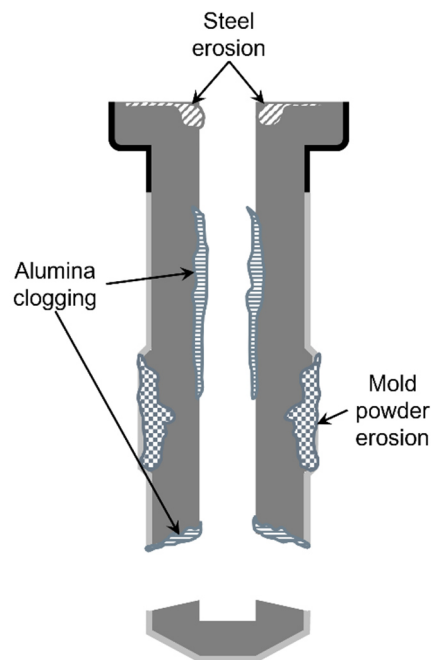


Figure 2-2: Schematic drawing of a submerged entry nozzle including typical wear mechanisms in different areas. Redrawn after [1]

2.4 State-of-the-art in wear detection

If focused on the wear detection on the inner surface of refractory shrouds, it must be stated that there is not really a measurement technique existing or state of the art. Usually, on the inner surface of submerged entry nozzles no wear is recognized. Instead clogging takes place, which is described in more detail later in this work. Besides that, the wear of the slag line is typically of much more interest than on the inner surface, which also applies in case of ladle shrouds.

Since there is no detection method for the wear of refractory tubes, the corrosion is usually tested beforehand. For this practice, no standardized tests exist but typically there are three methods which are currently used [1]:

- Crucible testing: slag samples are added in crucibles made of refractory material; the crucible is heated in a furnace until the slag melts.
- Finger testing: long “fingers” are made of refractory material and rotated in a bath of steel and/or slag at typical operating temperatures for a specified time.
- Rotary slag testing: a rotary kiln which is lined with refractory sample bricks is heated up to operating temperature, then steel or slag is inserted; then slag is added at varying intervals.

After these tests, the depth of dissolution and infiltration determines the corrosion resistance of the refractory material. [1]

Recently, a new method for refractory wear testing, the Continuous Wear Testing Device (CWTD) was developed. The exterior view and the furnace chamber of the CWTD at room temperature are shown in **Figure 2-3**. With help of this technique, in-situ wear rate measurements of refractory dissolution in slags are possible. [10]

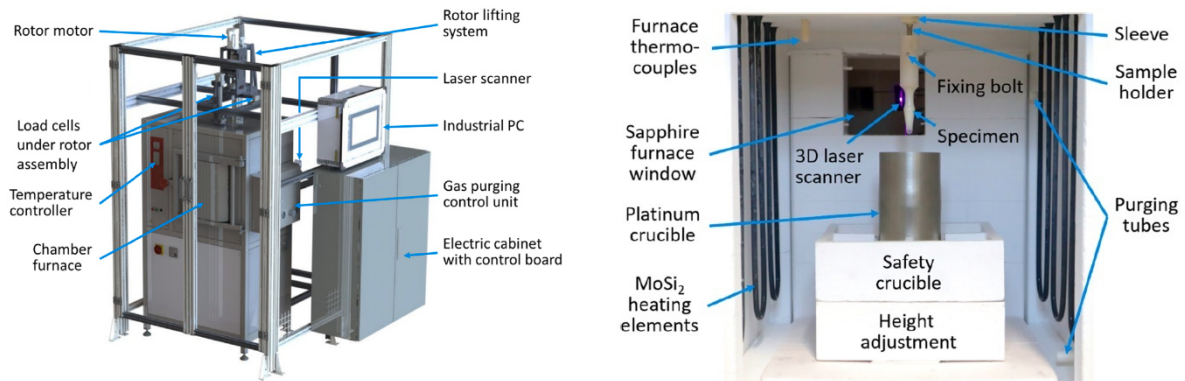


Figure 2-3: Exterior view (left picture) and furnace chamber of the Continuous Wear Testing Device at room temperature during measurement of an Al₂O₃ specimen (right picture). [10]

In literature, a method to characterize the wear of the slag line of submerged entry nozzles was established. With this technique it is not only possible to characterize the wear, but also a model to predict nozzle wear was developed. The wear profile of used SENs was measured with an automatic profilometer with digital acquisition, an example can be seen in **Figure 2-4**. On the left picture a typical wear profile of a used submerged nozzle is shown and on the right an example of the measurement results can be found. [11]

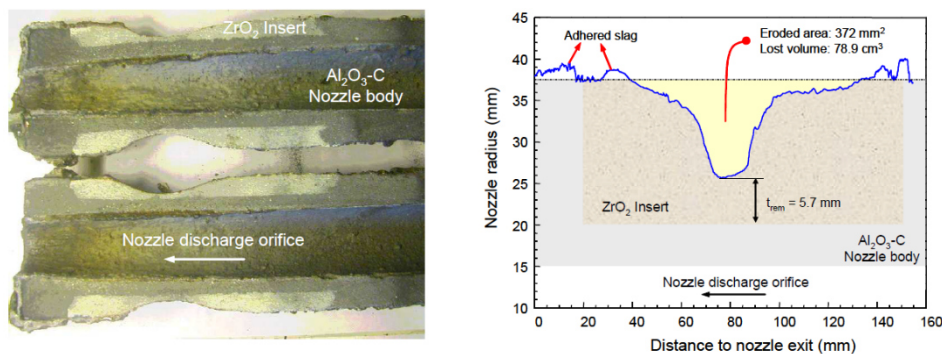


Figure 2-4: Characterization of the wear profile of submerged entry nozzles, left picture: typical wear profile of a used SEN, right picture: profile measurement result. [11]

2.5 Countermeasures

Since the lifetime of refractory tubes is very limited, plenty of countermeasures were developed over time. Some techniques are listed here [5,12]:

- Metallic additives (Al, Si) to reduce the CO formation due to oxidation, addition of Si reduces pore size, improves the permeability and abrasion resistance due to formation of SiC whiskers.

- ZrO_2 in the slag line area to prevent excessive wear due to penetration of slag thus improving the corrosion resistance, as well as in other high wear zones (e.g., on the top of the ladle shroud) to lower the abrasion.
- Increased wall thickness in the submerged part because this section is highly attacked by slag and molten metal.
- Application of a carbon-free inner liner which acts as a heat insulator and thus reduces thermal shock, as well as thermal stress at steel contact area.
- Optimising the cleaning technology by replacing the point cleaning (oxygen lancing) with face cleaning (oxygen shower) during ladle change.

3 Clogging

A build-up of material in the continuous casting process is referred to as clogging. Clogging is a phenomenon which can lead to severe problems regarding steel quality and productivity. Generally, clogging can occur in different areas in the process of steel casting, but mostly “nozzle clogging” is addressed in literature. Thereby, a build-up of material takes place in the ladle shroud or the submerged entry nozzle, the casting shroud from the ladle to tundish and tundish to mould respectively. This build-up consists, among others, of an agglomeration of non-metallic inclusions, which can adhere on the inner nozzle wall, solid steel build-up or reaction products which can occur during the reaction of liquid steel and refractory materials. In **Figure 3-1** an unused submerged entry nozzle, as well as a clogged SEN is shown. Another consequence is a decreasing nozzle diameter which leads to a decreasing flow rate. Furthermore, the flow pattern inside the shrouds is changed in such way that it can lead to a change in the flow inside the casting mould, resulting in slag inclusions and consequently in defects on the surface of the finished product. Additionally, a detachment of parts of the clogging material is possible, which can again lead to quality issues due to transportation of the detached clogging parts with the liquid steel into the finished product or by altering the chemical composition of the slag. [3,13–21]

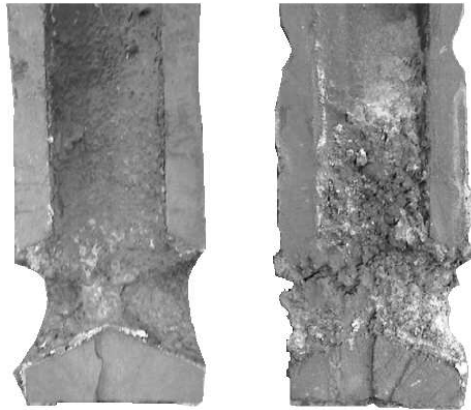


Figure 3-1: Left picture: submerged entry nozzle after a short time of casting, right picture: clogged SEN. [19]

As clogging is one of the biggest factors regarding lifetime of submerged entry nozzles, the following chapter deals with the mechanisms, the detection of clogging and countermeasures to minimize this problem.

3.1 Clogging mechanisms

In literature there are generally four types of clogging mechanisms mentioned. However, it is believed that clogging actually is a combination of two or more of these mechanisms. According to Rackers et al [3,13] and Thomas et al [14] these four clogging mechanisms can be named as follows [8,21,22]:

- transport of particles to a boundary layer and agglomeration of them,
- build-up of solidified steel,
- aspiration of air into/through the casting nozzle, and
- build-up of reaction products

In the following subchapters a short description of each mechanism is given.

3.1.1 Transport of particles to a boundary layer and agglomeration of these

The agglomeration and disposal of particles already existing in the steel before entering the nozzle is believed to be the main source of nozzle clogging. These particles or solid inclusions can originate from various sources, among them deoxidation products or slag entrapments. Therefore, to minimize the build-up of material in the nozzle, a reduction of the number of non-metallic inclusions is beneficial. Furthermore, it is advantageous to limit their transport and

attachment to the nozzle walls. This is possible by adjusting the flow pattern inside the nozzle. Misalignment of the shroud, turbulences, as well as fluctuations in casting speed are disadvantageous regarding the flow and should be avoided. Additionally, smooth nozzle walls were found to have a positive effect in increasing the thickness of the laminar boundary layer and therefore minimize the contact of particles with the nozzle wall. Detailed information regarding the formation of non-metallic inclusions (NMI) during steelmaking can be found elsewhere. [14,16]

3.1.2 Build-up of solidified steel

Another mechanism of nozzle clogging is the build-up of solidified steel. Steel can solidify at the beginning of casting if e.g., the preheating of the nozzle is insufficient, or the so-called superheat of the steel is low. Furthermore, if liquid steel gets trapped inside the clogging network it could possibly freeze due to a rather slow flow rate. These problems mostly occur if the superheat of the steel is rather low, as well as if the freezing range of the alloy is rather large. It has to be stated, that the solidification of steel on the nozzle wall at the casting start is not uncommon. This happens due to the temperature of the preheated nozzles, which is slightly below solidus temperature of the steel. Usually, this is not a big problem since the solidified layer is melting within a few minutes as the nozzle walls heat up. However, if another mechanism is initiated during this stage clogging may start. [3,13,14]

3.1.3 Aspiration of air into the casting nozzle

Through cracks within the refractory itself and joints between different parts of the flow control system a suction of air into the nozzle can occur. Hence reoxidation of steel takes place, which leads to a higher chance of nozzle clogging. The entered oxygen reacts with e.g., the dissolved aluminium present in the steel, forming solid aluminium oxide inclusions, which are the main source for nozzle clogging in steelmaking. Furthermore, the aspirated oxygen is believed to create a surface tension gradient near the wall, which can lead to a force accelerating non-metallic inclusions towards the nozzle wall. These tension forces are possibly the major effect of clogging in regions with low turbulences. The aspiration of air is more likely to occur, if the pressure inside the nozzle drops, creating a minimum pressure in some areas. This is also known as the “venturi effect”. [3,14,15]

3.1.4 Build-up of reaction products

According to literature also clogging material which rather looks like a uniform film than a sintered network is found. These films are also composed of deoxidation products but are believed to come from reactions of the refractory material with the liquid steel. Thereby, the aluminium in the steel reacts with oxygen coming from the refractory material e.g., if carbon monoxide is formed by reaction of the carbon with impurities or binders. Thus, creating an initiating layer of alumina on refractory surface. Additionally, in case of ladle slags with high FeO or MnO contents, the oxygen potential may be high enough to react with the aluminium in the steel to form Al_2O_3 . The modification of alumina inclusions with Ca (see also Chapter 3.3.3) can also deteriorate the clogging problems, if not conducted correctly. [3,13,14,17,22–25]

3.2 State-of-the-art in clogging detection

As clogging cannot be avoided completely in the steelmaking process it is no surprise that there are different methods to detect this phenomenon. Since there is no way to directly detect nozzle clogging several parameters are monitored on-line during casting. These are for example [14,18]:

- mould level fluctuations,
- argon back pressure if argon shrouding is applied within the casting system,
- nitrogen pick-up, and
- stopper rod movement or slide gate position.

A short overview about these methods, except nitrogen pick-up, is given in the subsequent sections. An increasing nitrogen content is an indicator for reoxidation problems during casting, which can cause clogging. Since there is no online method to detect the nitrogen pick-up during casting, it is not dealt with this method in more detail. [14]

3.2.1 Mould level fluctuations

Clogging of the nozzle bore leads to an increase of fluctuations of the metal level in the continuous casting mould, see also **Figure 3-2**. These fluctuations are the outcome of the attempt to maintain a constant metal flow rate if something changes inside the casting nozzle. These changes are for example the decrease of the nozzle diameter due to clogging. [14]

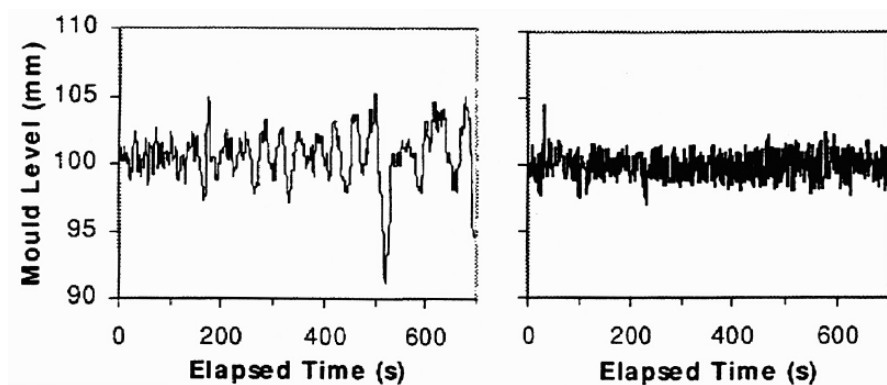


Figure 3-2: Mould level fluctuations due to clogging (left picture clogged SEN, right picture unclogged SEN) [14]

As small changes in the inner shape of the casting nozzle can lead to significant changes on the mould level, even initial clogging can be detected. Anyway it has to be stated, that this is not a reliable measurement method for clogging, as the mould level is prone to fluctuations caused by several other disruptions. [14]

3.2.2 Argon back pressure

Changes in argon back pressure indicate problems like the aspiration of air or blocking of the purging channel. **Figure 3-3** shows the pressure distribution in a standard tundish nozzle, which was calculated by a computational flow model. As the suction of air into the nozzle through joints or cracks can lead to formation and build-up of aluminium oxides, this method is a good indicator for clogging. [14]

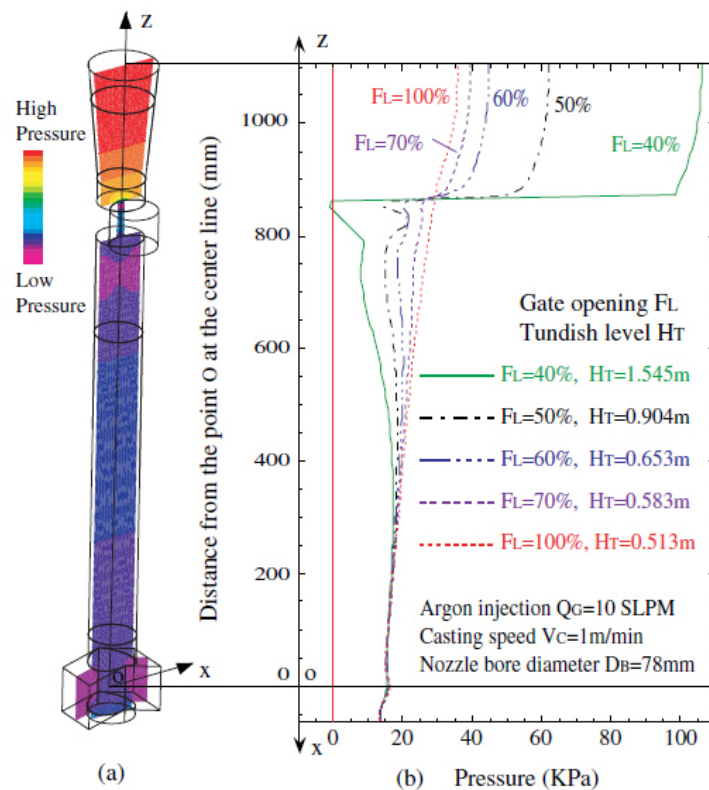


Figure 3-3: Pressure distribution in a standard tundish nozzle, which was calculated by a computational flow model. a) shaded contour plot, b) pressure profile along the centreline of the nozzle. [14]

3.2.3 Stopper rod movement or slide gate position

Clogging leads to a decrease of the nozzle inner diameter which limits the flow rate through this nozzle. In order to keep the flow rate constant during casting, the stopper rod or the slide gate must open up. This change of the position can be used to draw conclusions about the extent of the build-up of aluminium oxide inside the nozzle. An example of the change of the casting speed and the stopper rod movement can be seen in **Figure 3-4**. [14,26]

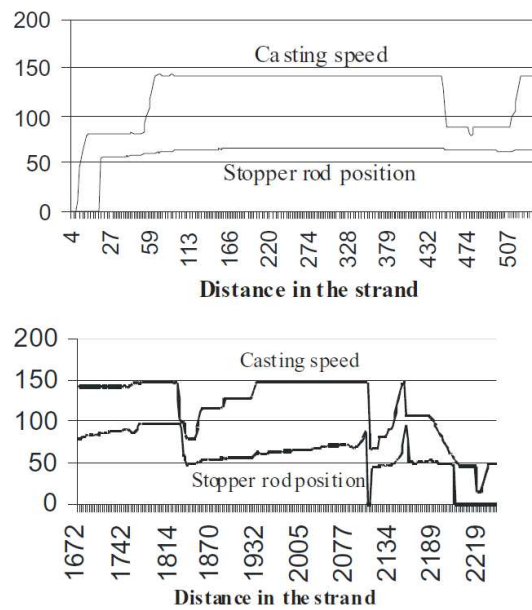


Figure 3-4: Casting speed and stopper rod position in case of an unclogged SEN (upper picture) and a clogged SEN (lower picture) [26]

3.3 Countermeasures

The most common methods to avoid or reduce the build-up of clogging material are [3,13,26]:

- production of steel with higher cleanliness (secondary metallurgy processes),
- argon purging of the nozzle or within the tundish to mould casting channel,
- modification of inclusions via calcium treatment,
- geometrical modifications of the nozzle, and
- modification of the nozzle material.

In the following subchapters these methods are described briefly.

3.3.1 Production of steel with higher cleanliness

As clogging material mostly consists of agglomerated non-metallic inclusions the most obvious way to reduce clogging is to increase the steel cleanliness in the liquid melt. Therefore, it is necessary to reduce the number of non-metallic inclusions which form during deoxidation or due to reoxidation. One method to reduce the number of NMI in the steel, is purging at very low flow rates in the ladle. This technique is called soft bubbling. Various types of purge plugs

are available in the market, among them the slot plug and the hybrid plug, for example. These purging plugs can be seen in **Figure 3-5**. [3,13,27,28]

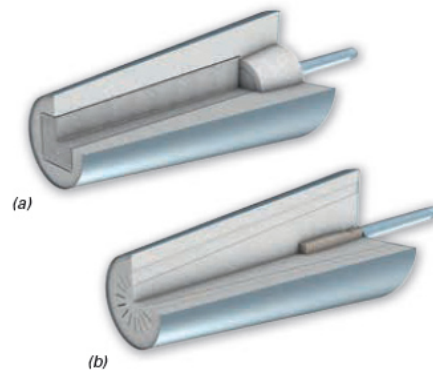


Figure 3-5: Two different purging plug types, (a) hybrid plug, (b) slot plug. [27]

If these two purging plugs are compared, the hybrid plug is the better choice for NMI removal. Since the slot plug is not good controllable at low flow rates, creating less but bigger bubbles than the hybrid plug, it is a rather poor solution. The slot plug however, shows a perfect operation at higher flow rates, necessary for homogenization, desulphurization, and alloying. Nevertheless, it is very doubtful that a higher steel cleanliness will completely avoid nozzle clogging. [3,13,28]

3.3.2 Argon purging within the casting channel

Another widely used method to reduce the build-up of oxides inside of continuous casting nozzles is the purging with argon. Thereby argon is injected either through the nozzle wall or the stopper rod into the liquid melt. Different theories deal with the question why the injection of argon leads to an improvement regarding nozzle clogging. The two most mentioned in literature are stated here:

- The argon gas is believed to form a film on the inner nozzle wall which prevents the contact between inclusions and wall. [3,13,14]
- Argon reduces the chemical reactions between refractory and the liquid melt by reducing the negative pressure at the nozzle inlet. Thus, minimizing the risk of air aspiration, which has a beneficial effect on the formation of aluminium oxide build-up. [3,13–15]

However, argon purging also comes with various disadvantages including higher erosion of the nozzle slag line because of higher level fluctuations in the mould, bubble entrapment on

the steel surface, as well as crack formation in the casting nozzle due to higher pressure or reduced thermal shock resistance. [3,13–15]

3.3.3 Modification of inclusions via calcium treatment

A treatment of the liquid metal with calcium is deployed to convert solid NMI into liquid inclusions. In more detail the high melting alumina inclusions should be modified into low melting calcium aluminates. This is realized by a modification of their chemical composition, which is favourable in terms of formation of a sintered network of inclusions. The reaction path of the modification of clustered alumina inclusions to calcium aluminate inclusions is shown in **Figure 3-6**. Here, clustered alumina inclusions were formed after the deoxidation of steel. Directly after the calcium addition, CaS adhering to the unmodified alumina was found. After some time the inclusion morphology was completely transformed to a spherical calcium aluminate inclusion, obtained by the reaction of CaS with alumina. [3,13,21,29–34]

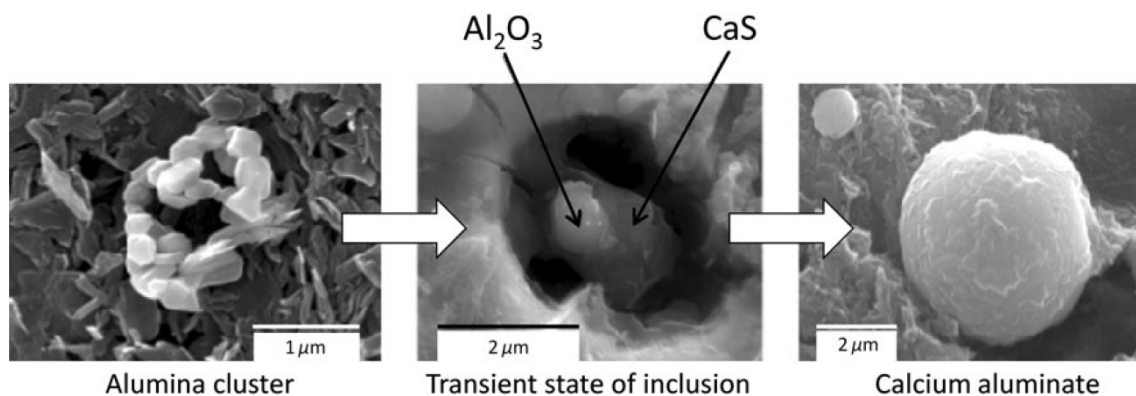


Figure 3-6: Modification route of alumina inclusions modified by calcium. [29]

Liquid non-metallic inclusions show a lower tendency to adhere to the inner wall of casting nozzles, thus a build-up of clogging material is reduced. Despite the benefits of calcium treatment, also some disadvantages can occur. Among them are for example the formation of CaS inclusions at higher sulphur contents, as well as the formation of CaC_2 in case of high carbon steels. These inclusions can again lead to a higher clogging tendency. [3,13,21,29–34]

3.3.4 Geometrical modifications of the nozzle

Numerous geometrical modifications are applied to reduce clogging, including:

- Improved sealing of joints and slide gate closures to reduce air aspiration into the casting nozzle and thus minimize clogging. [3,13]

- Rounded inlet of the casting nozzle optimizes the flow at this area and thereby reduces material build-up. [3,13,35]
- Step nozzle design leads to a reduction of clogging in the lower part of the nozzle as well as a reduction of the influence of the flow pattern inside the mould. [3,13,16,25]
- A variable inner nozzle diameter changes the flow pattern, thus avoids areas with low flow speeds. [3,13,35]
- Insulation and preheating of the nozzle were also found to reduce the build-up of clogging material which can be caused by solidified steel. [3,13]

3.3.5 Modification of the nozzle material

There also have been several considerations regarding the modification of the refractory material of the casting nozzle. This is achieved either by changing the material of the whole nozzle or by addition of a special coating on the inside. Calcium addition to the refractory material as well as a carbon-free liner on the inside of the nozzle are examples for these approaches. Also, boron nitride was found to be beneficial regarding the decreasing of clogging. However, it is not clarified if this positive effect is due to decreased surface roughness, the development of a liquid boron oxide film, or another cause. In addition, coating the nozzle walls with pure alumina and the control of the composition of the nozzle (e.g.: avoid Na, K and Si impurities), as well as zirconia linings are also used. Thereby, either less wetting of the refractory material or more inert surfaces should be achieved. Also, a decrease of thermal conductivity is believed to reduce clogging. Furthermore, the absence of carbon was found to be advantageous in terms of anti-clogging solutions. [3,13,16,17,22,23,25]

4 Overview on temperature measurement

In general, there are two methods to measure the temperature of an object [36]:

- the contact temperature measurement e.g., thermocouples, and
- the non-contact temperature measurement e.g., radiation thermometers.

The types of radiation thermometers are manifold, including optical and photoelectrical pyrometers, total radiation thermometers, fibre optic thermometers, total radiation thermometers, infrared radiation thermometers, etc. [36]

4.1 The principle of radiation thermometers

In general, every object with a temperature above absolute zero is emitting electromagnetic radiation. This characteristic radiation is dependent on the temperature of the object and due to internal mechanical movement of the molecules. With rising temperature of the material, the intensity of the emitted radiation energy is also rising. The electromagnetic spectrum including the used range of the infrared radiation can be seen in **Figure 4-1**. [37–46]

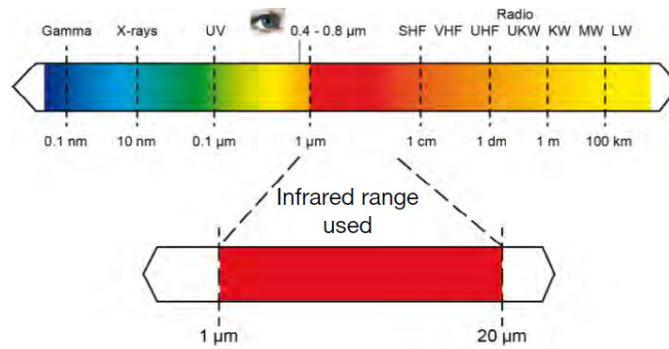


Figure 4-1: Electromagnetic spectrum including the used range of the infrared area. [46]

The measurement principle for all the used non-contact temperature measurement techniques is the same and is based on Planck’s law of radiation. For the electromagnetic radiation of a black body the Planck’s law can be described by **Equation (4-1)**. [36,39,40,45,47–54]

$$M_{\lambda} = \frac{c_1}{\lambda^5} * \frac{1}{\exp\left(\frac{c_2}{\lambda T}\right) - 1} \quad (4-1)$$

M_{λ}spectral radiance of the black body

c_1first radiation constant (= $3,7418 * 10^4 \text{ W*cm}^{-2}*\mu\text{m}^4$)

c_2second radiation constant (= $1,4388 * 10^4 \text{ K*}\mu\text{m}^4$)

T.....temperature of the measured black body

λwavelength in vacuum

In **Figure 4-2** the electromagnetic radiation of a black body at different temperatures over the wavelength is shown. As can be seen in this figure, materials are emitting electromagnetic radiation in the infrared spectrum also at very low temperatures. Furthermore, the maxima of the radiation curves are shifted towards lower wavelengths with higher temperature and the curves show no overlapping at any wavelength or electromagnetic radiation. At higher temperatures there is a small area where materials emit radiation in the spectrum of visible light, which appears as glowing in red to white colour. [37,40,41,46]

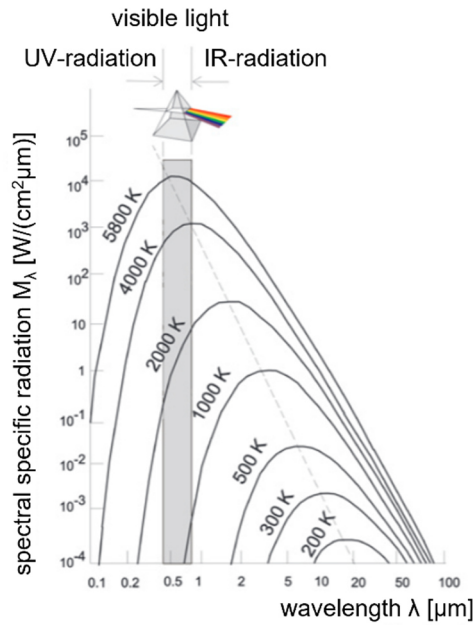


Figure 4-2: Electromagnetic radiation of a black body over the wavelength for different temperatures. [40]

However, **Figure 4-2** is only valid for black bodies. Many bodies only emit a fraction of the electromagnetic radiation at the same temperature compared to black bodies. The link between the real radiation and the radiation of a black body is defined as emissivity ϵ , which can have a value between 1 and 0. For black bodies ϵ reaches the maximum of 1. Grey bodies emit less radiation and are defined by a constant emissivity and an independence of the wavelength. Whereas the emissivity of real bodies, also called non-grey bodies, is dependent on temperature and wavelength. In **Figure 4-3** the specific electromagnetic radiation at different emissivity can be seen. [38,40–42,46,50,55,56]

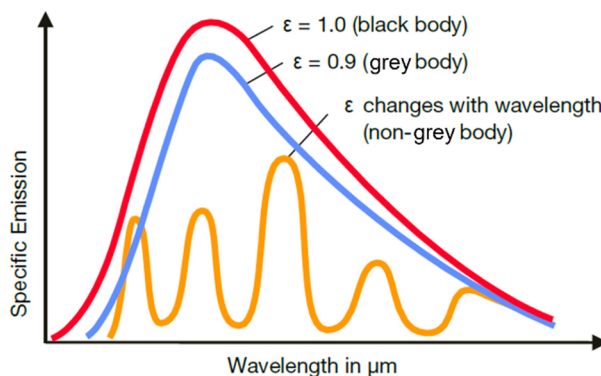


Figure 4-3: Specific electromagnetic radiation at different emissivity for a black body, a grey body and a non-grey body. [46]

The emissivity ϵ of a real body can be calculated using **Equation (4-2)** [40,41]:

$$\epsilon(\lambda, T) = \frac{M_{\text{real}}}{M_{\text{black body}}} \quad (4-2)$$

ϵemissivity of the real body

M_{real}radiation of the real body

$M_{\text{black body}}$radiation of the black body

It is common practice to treat non-grey bodies as grey bodies, as the emissivity can be considered as constant within short wavelength ranges. But this assumption is not valid for gases or liquids. [41]

In this work, a pyrometer, an infrared camera, a broadband spectral thermometer (BST), as well as thermocouples were used. Therefore, the measurement principles of these devices are explained more detailed in the following subchapters.

4.2 Pyrometer

If speaking of pyrometers, it must be distinguished between optical and infrared pyrometers. Optical pyrometers measure the temperature by comparing the brightness of an object in the visible spectrum to a known brightness of an internal lamp. Whereas the latter is measuring in the range of the infrared spectrum. In both groups, the optical and the infrared pyrometers, two different types are available respectively. Photoscrenic wedge-type and disappearing-filament pyrometers in the optical group, and single wavelength (also single colour) and multiple wavelength (also multicolour) in the infrared group. In this work an infrared pyrometer was used, therefore this group is described in more detail. [44,57]

Infrared thermometers can measure a broad temperature range of approximately - 20 °C – 4000 °C and are therefore suitable for the usage in various application fields. These types of pyrometers are measuring typically in very broad or very narrow bandwidths. Usually, broad-bandwidth pyrometers can measure a much broader range of temperatures compared to narrow-bandwidth pyrometers. Unfortunately, this means that these pyrometers are affected by the emissivity to a greater extent. This is because the emissivity is dependent not only on the temperature but also on the wavelength. In **Figure 4-4** the measurement spectrum of a broadband single colour pyrometer can be seen. Optical phenomena can affect the spectrum in different ways. Hence, atomic emission for instance can lead to peaks in the spectrum (see blue marked areas in **Figure 4-4**). On the other hand, absorption may result in minima (green

marked areas). The measured intensity is then used to determine the temperature of the object. In case of single colour pyrometers only one single segment of the spectrum or wavelength is measured. If a rather small segment is used for the measurement and the spectrum shows a lot of peaks and minima, there is a high risk for measurement inaccuracy. This method cannot only be used for broad-bandwidth pyrometers but also for narrow-bandwidth pyrometers. [44,50,58]

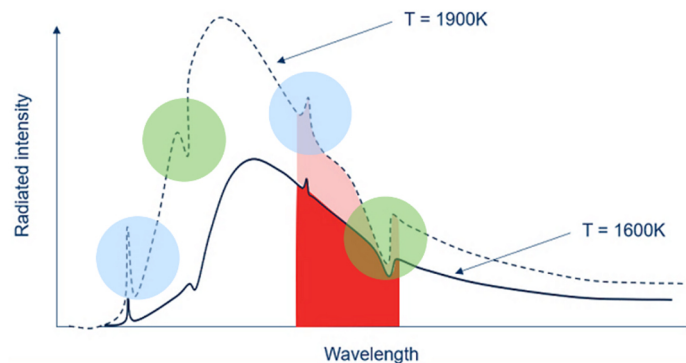


Figure 4-4: Measurement spectrum of a broadband single colour pyrometer. Red area shows the wavelength range which is measured. [58]

In case of the narrow-bandwidth pyrometers, the variation of the emissivity is not the limiting factor. Indeed, the emissivity to measure the temperature with a narrow bandwidth pyrometer must also be known, but usually it stays nearly the same if only a very small range of wavelengths is measured. This can also be seen in **Figure 4-5**, where the measurement spectrum of a narrow-bandwidth dual wavelength pyrometer is shown. Here, the ratio of the two measured intensity values (I_{λ_1} and I_{λ_2}) is used to identify the temperature. Multiple wavelength pyrometers (or in case of **Figure 4-5** dual wavelength) are measuring in two or more segments of the spectrum. Hence, if the segments are close to each other, they should have theoretically the same emissivity value. Due to this, a ratio of 1:1 of the ϵ -values is reached, and it is possible to eliminate the emissivity mathematically and the measurement is no longer dependent on ϵ . In practice however, this is often not the case, which can lead to significant errors regarding temperature measurement. Again, if the intensity is measured at a peak or a minimum of the spectrum, measurement inaccuracies can occur. In contrast to the single colour pyrometer however, it is likely to reduce these errors since two or even more intensities are measured. Hence, there is the possibility that these maxima and minima are balanced. [44,48,50,52,54,58,59]

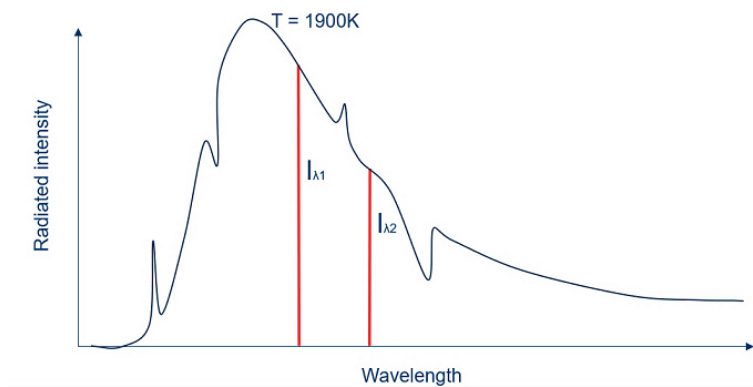


Figure 4-5: Measurement spectrum of a narrow-bandwidth dual wavelength pyrometer. Red lines show the wavelengths, at which the intensity was measured. [58]

4.3 BST (broadband spectral thermometer)

The broadband spectral thermometer (BST) represents an industry 4.0 initiative from RHI Magnesita to enable contactless temperature measurement, which is independent from the measured material, as well as from the emissivity coefficient ϵ . In **Figure 4-6** the measurement spectrum of the BST, as well as the fitted or calculated black body curve at 1900 K are shown. [58]

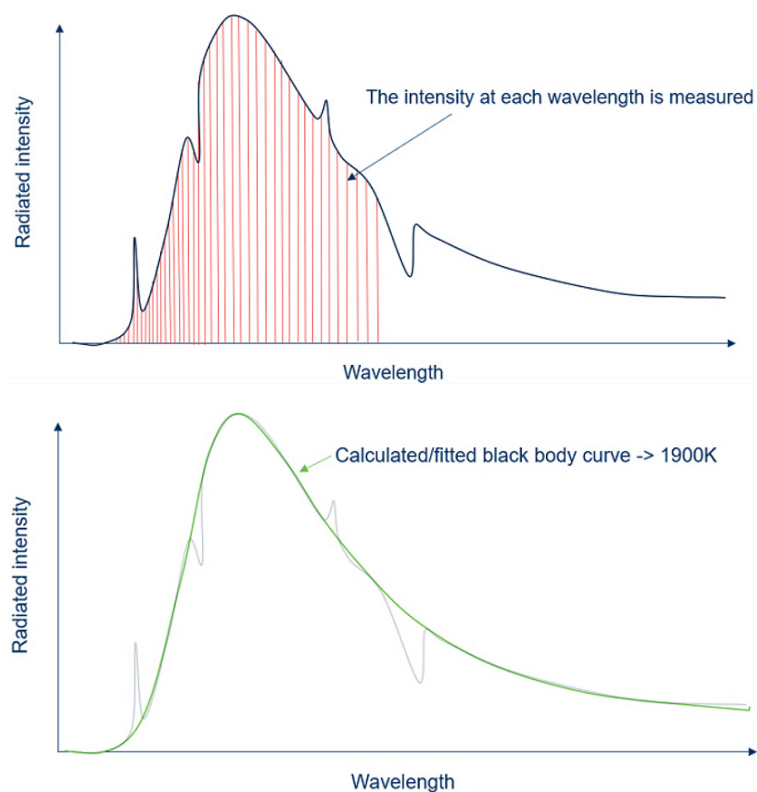


Figure 4-6: Measurement spectrum of the BST (upper picture) as well as the calculated/fitted black body curve at 1900 K. [58]

In contrast to standard pyrometers (see also **Chapter 4.2**), the BST measures the intensity at each wavelength, which leads to a calculated or fitted curve. Here, the whole shape of the spectrum is considered for the evaluation of the object temperature. Therefore, the before mentioned peaks and minima do not affect the measurement. [58]

4.4 Infrared camera

Infrared cameras have the same working principle as pyrometers. Both belong to the infrared thermography (IRT). However, infrared cameras are more sophisticated than pyrometers, as they are able to produce a detailed infrared image. These are established by converting the infrared radiation into a visible image, relating each infrared energy level to a colour. The outcome is a false colour image, which is also named a thermogram. The basic structure of an infrared (IR) camera is relatively similar compared to a conventional camera. The main difference is the detection of infrared radiation instead of visible light. Thus, different lenses are used for infrared cameras because normal glass is not permeable for infrared radiation. Typically, the glass lenses are replaced by germanium, for example. [37,40,41,43,45,60]

IR cameras are categorised according to their camera systems. There are two systems: the scanning cameras and the focal plane array (FPA) cameras. [40,45]

Scanning cameras consist of only one detector unit. Therefore, an “optomechanical deflection system” is needed, which scans the whole area by scanning it like a grid. These camera systems have a high thermal resolution, but it takes long to produce a thermogram because the scanning of each pixel is quite time consuming. The functional principle of scanning cameras can be seen in **Figure 4-7** on the left side. [40]

FPA cameras have a detector matrix consisting of many receiver sensors. The whole infrared radiation is focused on this detector matrix, which leads to a quicker generation of the thermogram. Each sensor corresponds to one pixel in the thermogram. Since this system enables a very quick image sequence, it has recently become the dominating infrared camera system. In **Figure 4-7** the functional principle of FPA cameras is shown. [40]

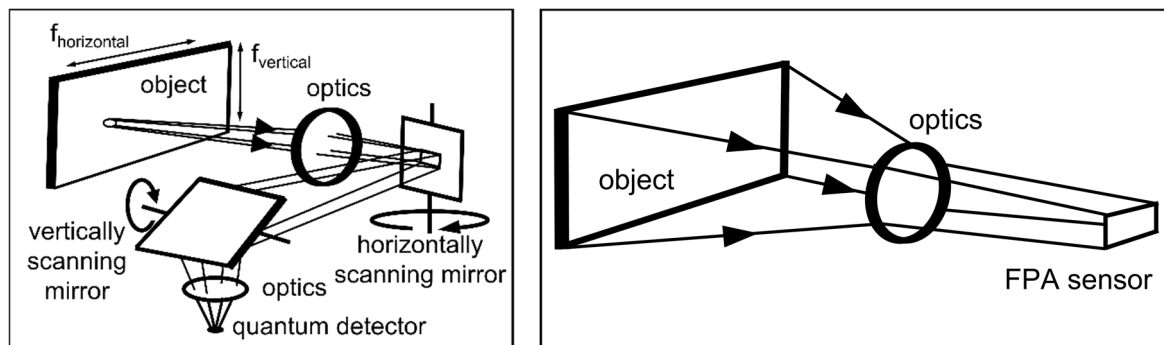


Figure 4-7: Functional principle of scanning cameras (left side) and FPA cameras (right side). Redrawn after [61]

Furthermore, it is distinguished between two different detectors. These are thermal detectors and quantum detectors. [40,45]

Thermal detectors are heated directly by the incoming radiation. This leads to a change in the electrical signal, which can be evaluated with the help of a computer. Thus, a thermogram can be created. No cooling is needed for this kind of detector. It is mainly used for focal plane array cameras. A schematic of a thermal detector can be seen in **Figure 4-8** on the left side. [40,45]

Quantum detectors, however, use the interaction between the material and the radiation for signal evaluation. This means that this detector acts like photon counter. It has to be stated, that cooling is required, as quantum detectors operate at very low temperatures of approximately 77 K. Apart from that, with this type of detectors a very fast measurement is possible. In **Figure 4-8** on the right side the schematic of a quantum detector is shown. [40,45]

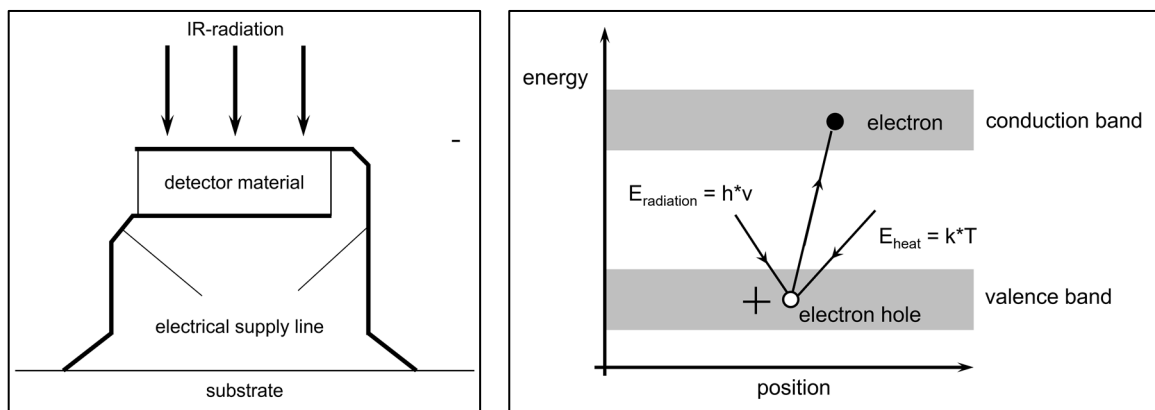


Figure 4-8: Schematic drawing of the functional principle of a thermal detector (left side) and a quantum detector (right side). Redrawn after [40]

Several parameters can affect the measurement. Among them are, for example, the emissivity and the moisture of the object to be measured, the distance of the object from the IR camera, the measurement angle, the air quality, as well as other sources of radiation. To give some examples of other sources of radiation, heating elements e.g., the oven, or heat from lamps must be mentioned. [41,51,60]

Nowadays, also affordable IR cameras are available. But they are still a very expensive measurement device. Furthermore, thermograms are rather difficult to interpret. Thus, a specific training is beneficial. [41]

4.5 Thermocouples

For contact temperature measurements thermocouples are very commonly used. This is due to their wide measuring range of $-270\text{ °C} - 3000\text{ °C}$, as well as their low cost, robustness, size, and simplicity. The measurement principle of thermocouple is attributed to the Seebeck effect. This effect describes the production of an electromotive force (EMF), if two dissimilar conductors in one circuit are exposed to a thermal gradient. It is distinguished between four different groups [62]:

- noble metal,
- base metal,
- high temperature or refractory metal, and
- nonmetal.

Noble metals are used because of their chemical stability, as well as their thermoelectric power. Although noble metals are known to be relatively inert, platinum oxidizes at 600 °C. Copper, nickel, aluminium, iron, and chromium, as well as their alloys, are in the group of base metals. These can be used to produce materials with preferable thermoelectric characteristics, e.g., constantan and chromel. This kind of thermocouples are used preferably for low and moderate temperatures. Whereas, refractory metals, e.g., tungsten, rhenium, some of their alloys, as well as molybdenum, are used for high temperature measurement. However, these metals tend to oxidize very easily. Carbon, boron, as well as carbide and boride compounds are typically brittle and belong to the group of nonmetals. Furthermore, they have low tensile strengths. Usually, nonmetal thermocouples result in quite big composite rods. An overview about a few well-established standardized thermocouples is given in **Table 4-1**, which can be found in Chapter 4.6. [62]

For some applications, it can be necessary to isolate the thermocouples electrically or chemically from the surroundings. This is realized using different materials, including PVC, glass fibre polyimide, metal coatings with mineral insulation, and for higher temperatures, ceramic coatings. Measurement uncertainties can be promoted by cold junction temperature measurement, voltmeter sensitivity, and cable drift, among others. Cable drift is due to annealing of the thermocouple materials at high temperature applications and is known to be a usually occurring problem. [62]

4.6 Summary of temperature measurement methods

A summary of the key factors of the before mentioned temperature measurement methods is given in **Table 4-1**. More information can be found in the literature.

Table 4-1: Evaluation of temperature measurement methods.

device	IR camera	pyrometer	BST	thermocouples
absolute temperature	no [58]	yes / no [58]	yes [58]	yes [58]
temperature range	-20 – 3000 °C [63]	-20 – 4000 °C [44]	above 1000 °C [58]	-270 – 3000 °C [62]
measurement principle	optical [58]	optical [58]	optical [58]	contact
emissivity sensitivity	yes [58]	yes / no [58]	no [58]	no
measurement quality indication	yes / no [58]	no [58]	yes [58]	no
cost	€€€ [38]	€€ [38]	n.a.	€ [38]
limitations	everything in line of sight disturbing the view [64]	everything in line of sight disturbing the view [64]	n.a.	n.a.
	cleanness of optics [64]	cleanness of optics [64]	cleanness of optics [64]	n.a.
	n.a.	n.a.	n.a.	intrusive [64]

5 Experimental

To evaluate a potential use of contactless temperature measurement set-ups to detect clogging or wear of refractory pipes a special experimental test procedure was developed. Therefore plates of a typical material (see also **Table 2-2**, later referred to as ISO material) for ladle shrouds and submerged entry nozzles were manufactured. The temperature of these plates was measured during heating up with the help of a pyrometer, an IR camera, and the BST. Additionally, thermocouples were used as a reference.

5.1 Experimental set-up

In **Figure 5-1** a schematic of the experimental set-up for the laboratory trials is shown. On the left side the intersection of the furnace can be seen. Here, the sample of Clogging (later referred to as "C") (see also **Chapter 5.2**) was used to explain the set-up. On the hot side a clogging layer was attached, the middle part consists of ISO material, and an insulation layer is placed on the cold side. The furnace door was replaced by a refractory frame, leaving an opening of 120 x 120 mm. During the preheating of the furnace a dummy-plate was used to close this opening and minimize heat losses. Furthermore, a hole was drilled into the frame to achieve a possibility to flush the furnace with argon during the tests. This can be seen on the right side of **Figure 5-1**. To ensure a minimum of oxygen suction into the furnace, an insulation layer was placed around three sides of the samples. The temperature of the sample was measured during heating up. All three measuring devices (IR camera, pyrometer, and BST) were focused on the middle of the sample, see also the red point on the right side of **Figure 5-1**.

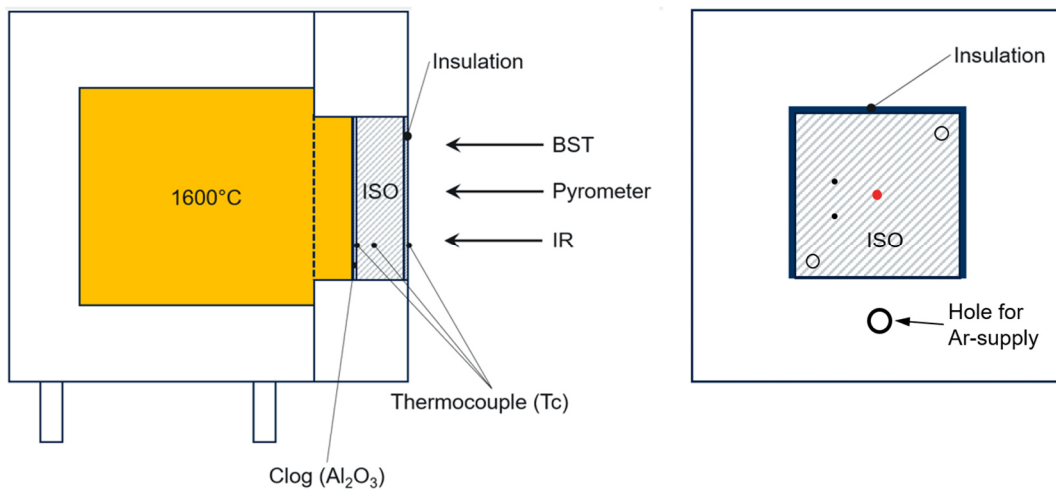


Figure 5-1: Schematic of the experimental set-up for the laboratory trials. On the left side the intersection of the furnace is shown, on the right side the front view of the refractory frame including the sample and the drilled hole for the argon supply can be seen.

The used infrared camera was a FLIR A615 (see also [65]), whereas the pyrometer was from Sensortherm, model Metis M3 (two-colour pyrometer, more information can be found in [66]). The BST is, as mentioned before, is an industry 4.0 approach from RHI Magnesita. Additionally, three thermocouples were used during each trial. Originally, all of them were supposed to be type N thermocouples, but during the trials one of them was replaced by a type S thermocouple. This was necessary due to the temperature reached near the hot face of the sample, which was higher than expected. The used devices as well as the actual set-up can be seen in **Figure 5-2**.

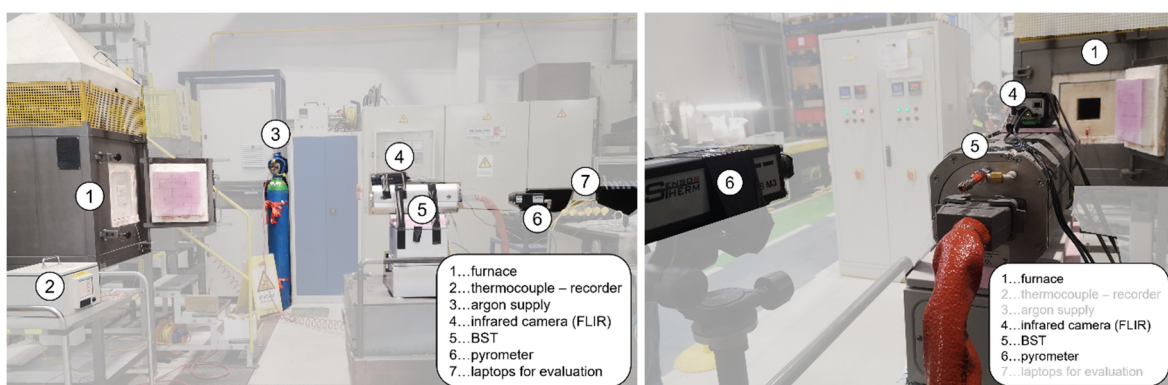


Figure 5-2: Experimental set-up for the laboratory trials.

The key parameters of the experimental set-up can be found in **Table 5-1**.

Table 5-1: Key parameters of the experimental set-up.

device	distance from sample	emission coefficient
IR camera (FLIR)	1.7 m	$\varepsilon = 1$
pyrometer	2.4 m	$\varepsilon_1/\varepsilon_2 = 1$
BST	1.7 m	-

5.2 Sample design and instrumentation

The samples were manufactured using an ISO material, which is typically used for ladle shrouds and submerged entry nozzles. In **Figure 5-3**, the design and dimensions of the plates are shown.

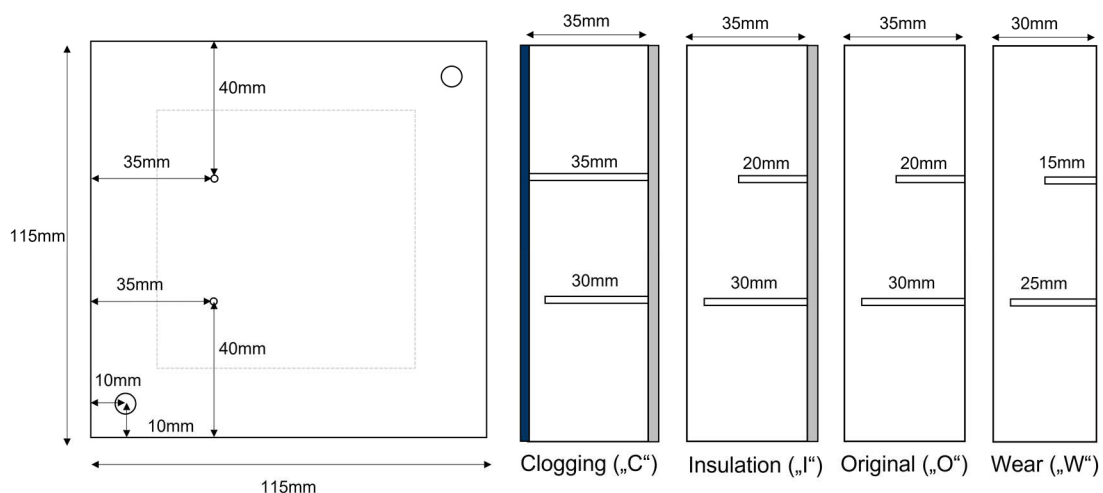


Figure 5-3: Sample design and dimensions. Clogging (“C”) refers to a clogged submerged entry nozzle, Insulation (“I”) illustrates a SEN without clogging, Original (“O”) represents an original ladle shroud without wear, and Wear (“W”) should indicate wear in case of a ladle shroud.

There are four different cases. Clogging (“C”) refers to a clogged submerged entry nozzle sample with insulation on the outside. Here, the dark blue area shows the build-up material, whereas the light grey area is the insulation. Between these two areas, the isostatically pressed body material of refractory tubes is illustrated. In case of Insulation (“I”), which should represent a submerged entry nozzle without clogging, again the grey area shows the insulation material. Original (“O”) represents an original ladle shroud without wear. Finally, Wear (“W”) stands for the measurement of wear and should illustrate a worn ladle shroud. This is realised by a thinner body material. For the simulation of a clogging layer, a refractory castable, which consists of

80 - 100% Al_2O_3 , was used. The isolation material is a so-called AES wool, whereby AES means alkaline earth silicate. This type of insulation material is typically used for submerged entry nozzles.

Furthermore, on the upper right and the lower left corner holes were drilled for the manipulation of the plates with the help of a calliper. Additionally, the drilling of smaller holes on the left side of the sample were necessary to insert thermocouples. These holes were drilled with different depths for each case, as can be seen in **Figure 5-3**, to measure the temperature inside the plates. Additionally, a thermocouple was placed on the surface of the sample.

To ensure a good insulation around the sample and in addition a reduction of air ingress, insulating wool was adhered to three sides of the plates. This is illustrated in **Figure 5-4**.

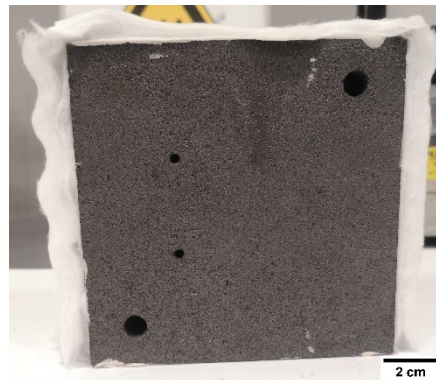


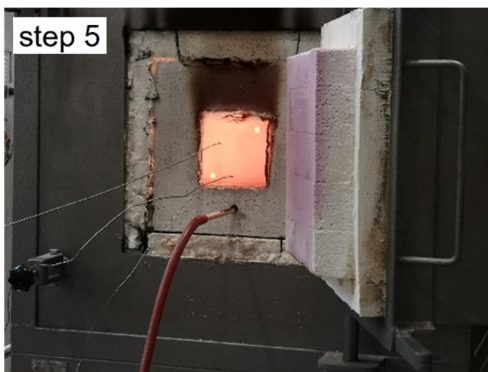
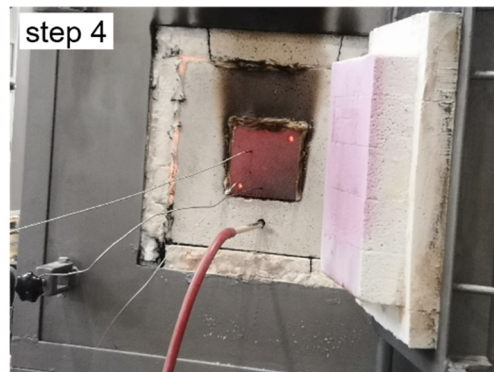
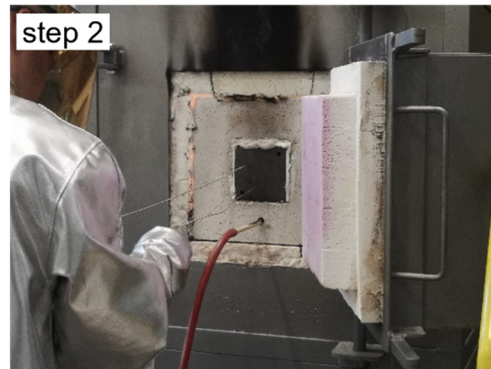
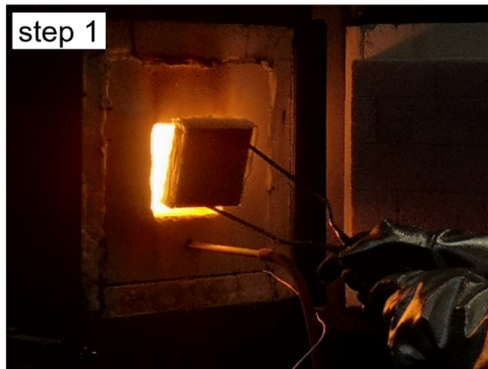
Figure 5-4: One sample of “W” with insulating wool on three sides, ready for laboratory trial.

5.3 Test procedure

The procedure of the laboratory test started by the preheating of the furnace to 1600 °C. After this, the dummy plates inside the refractory frame were removed to reopen the opening for the samples. The procedure can then be divided into six steps, which can also be seen in **Table 5-2**:

1. Inserting of the sample into the opening of the refractory frame.
2. Placing of the thermocouples in the holes and on the surface of the plate.
3. The sample starts to smoke, which stops after approximately 2 minutes.
4. The sample starts to glow.
5. The sample glows at the maximum temperature.
6. Removing of the sample from the furnace.

Table 5-2: Procedure of the laboratory tests.



6 Results and discussion

After the laboratory trials a visual rough inspection of the samples was done at first. Furthermore, some pictures were made with the help of a reflex camera and a macro-object lens. Afterwards, one sample of each case was cut, to examine the material condition on the inside of the sample. Finally, the data of the temperature measurement devices was evaluated, resulting in temperature profiles. These results are summarized and discussed in the following subchapters.

6.1 Physical sample analysis

In **Table 6-1** the samples before and after the laboratory trials can be seen. Additionally, pictures of the hot samples directly after the trial and the inside of the samples after the trials are shown. The pictures of each sample and case can be seen in **Chapter A** in the appendix.

Table 6-1: Overview of the samples before the laboratory trials.

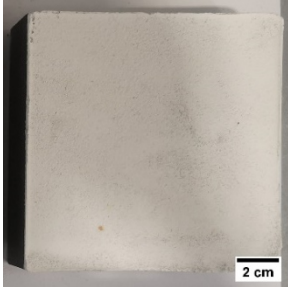
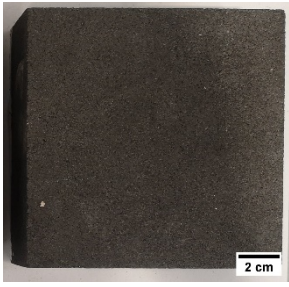
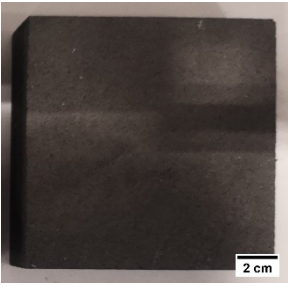
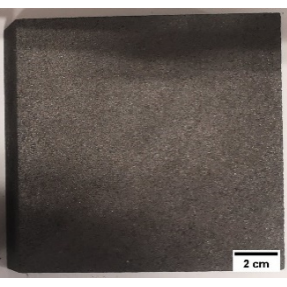




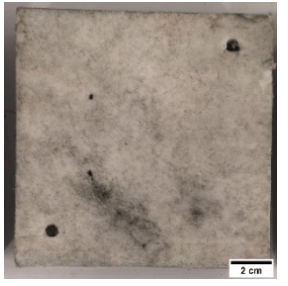
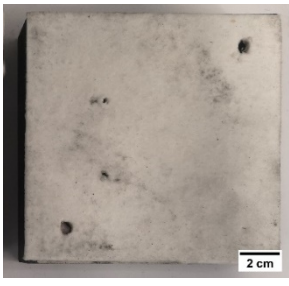
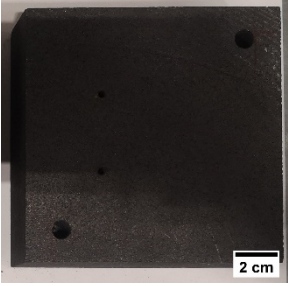
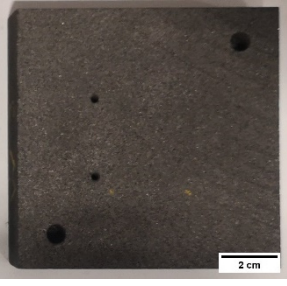
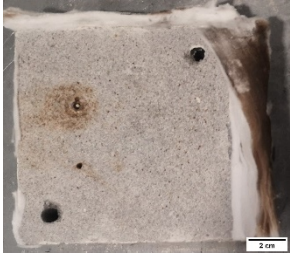
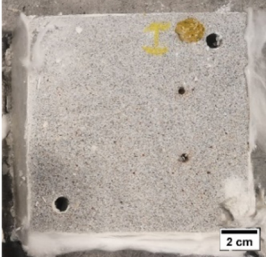
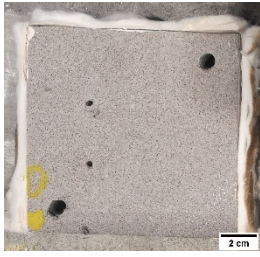
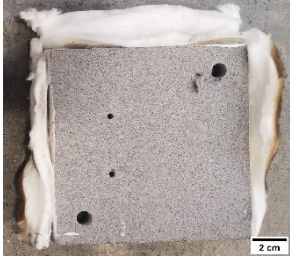

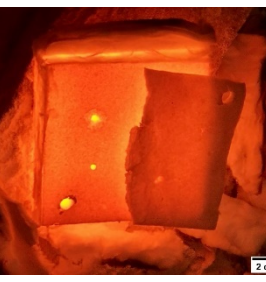
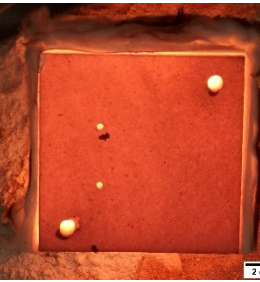

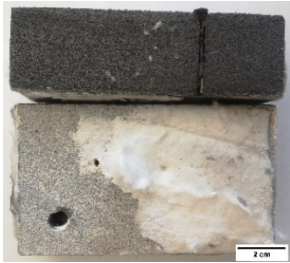
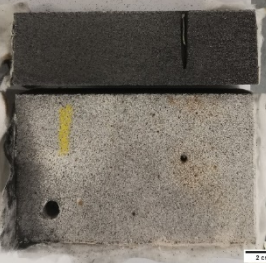
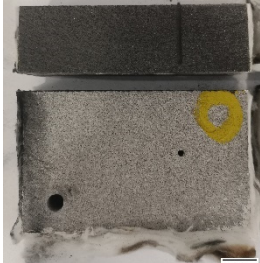
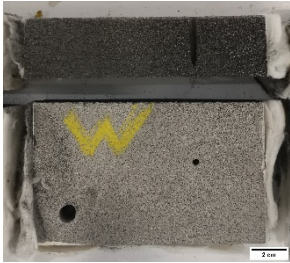
Clogging	Insulation	Original	Wear
Hot face, before trial			
			
Side face, before trial			
			
Cold face, before trial			
			

Table 6-2: Overview of the samples after the laboratory trials.

Clogging	Insulation	Original	Wear
Cold face, after trial			
			
Hot sample			
			
Cut sample			
			

In case of “C” and “I”, the images after the trial clearly show that the insulation of the samples had no perfect connection on the surface. However, it must be said that it did not fall off until the samples were removed and therefore no influence on the measurement is expected. Also, the clogging layer was detached from the samples, which can be seen in **Figure 6-1**, whereas it is not clear if it detached during the laboratory trial or during the sample exchange. In the left picture, the hot sample directly after the laboratory trial is shown, whereat the detached clogging layer is leaning on the left side. The right picture shows hot face of the cooled sample after the trial without the clogging layer. Here, it is not possible to give a statement about the time of the detachment.

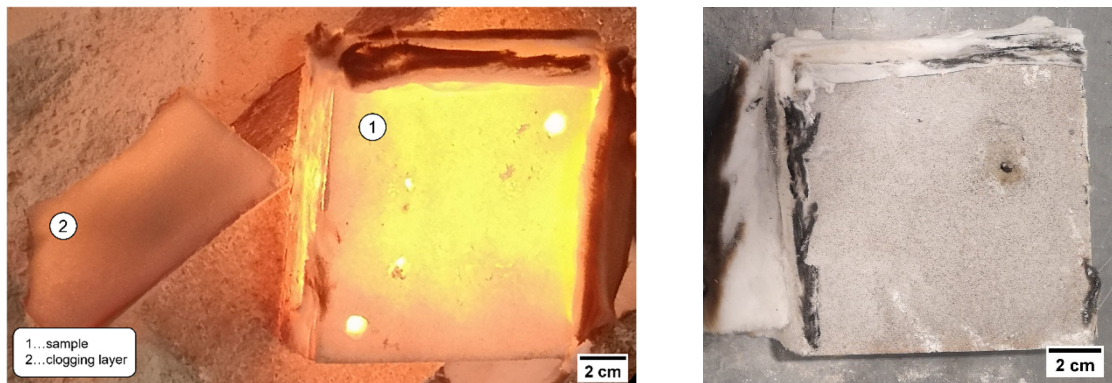


Figure 6-1: Hot sample of case “C” directly after the laboratory trial with detached clogging layer besides (left picture). Hot face of the sample after cooling without the clogging layer (right picture).

Furthermore, it is clearly visible because of the white surface colour, that during the laboratory trials at least some amount of decarburization occurred. But if a closer look is taken on the cut samples, it can be seen that the decarburization is limited to the surface. In **Figure 6-2** details of the cut sample of “I” are shown. On the left side the cold face is pictured, whereas on the right side the hot face of the sample is depicted. It is clearly visible, that the layer of decarburization on the surface of the cold face is thicker than on the hot face, which is also illustrated with the red marked areas in **Figure 6-2**. Thus, it can be stated that the flushing of the furnace with argon worked as expected, whereas the constant contact with ambient air results in a higher decarburization, even if the temperature of the outer surface is lower.

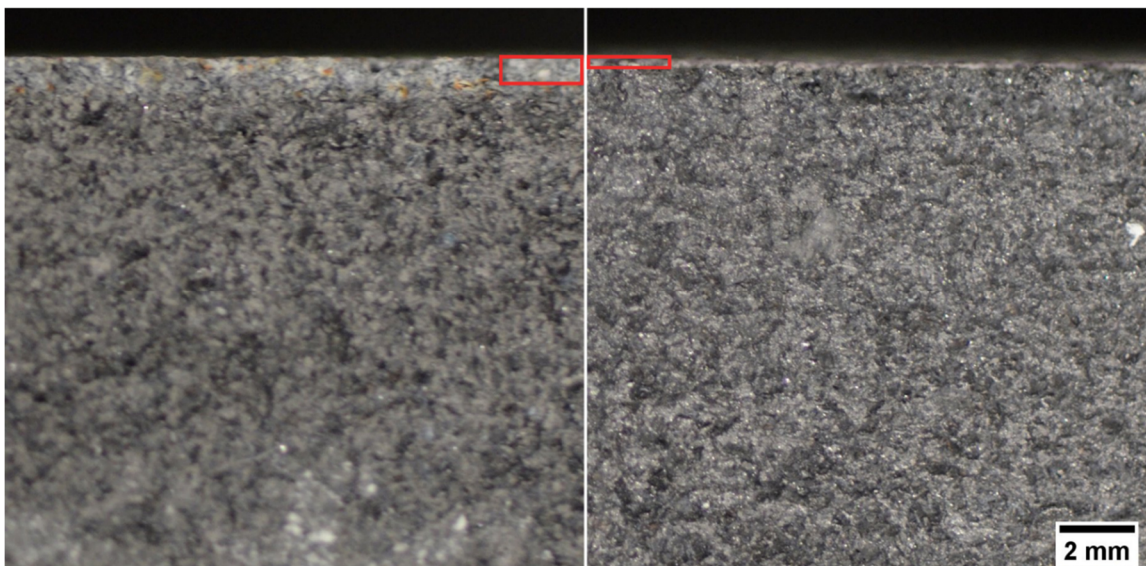


Figure 6-2: Details of the cut sample of “I”. On the left side the cold face is shown and on the right sight the hot face can be seen. In addition, to illustrate the difference in thickness, an area of the decarbonized layer is marked with red areas.

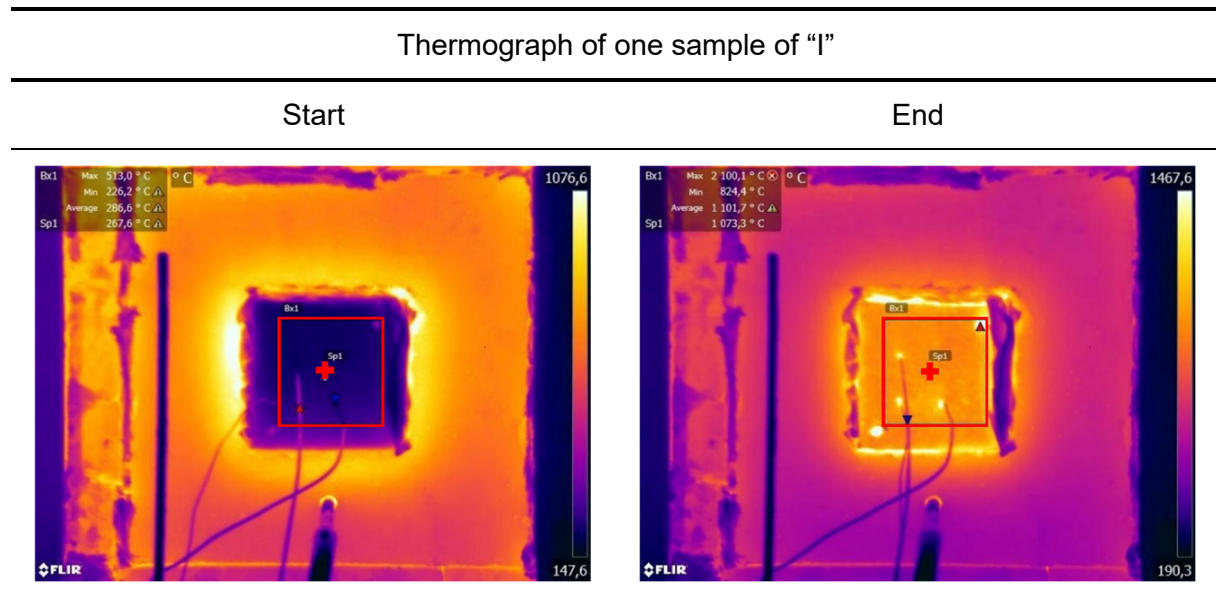
6.2 Temperature profiles

In the following subchapters the temperature profiles of the different measurement systems are shown and discussed in detail. Generally, the profiles for each sample were plotted in a diagram, before summarizing them into one mean curve including the standard deviation for each case. Finally, the mean curves for all cases are compared in another figure to point out the differences between the cases. To check whether the measurement time was long enough to ensure a constant temperature, the gradient ($\Delta T/\Delta t$) was calculated and plotted for the mean temperature curves obtained by the infrared camera FLIR A615. This can be seen in **Table B-1** in the appendix, **Chapter B**.

6.2.1 Infrared camera (FLIR)

Table 6-3 contains the thermographs at the start and the end of the laboratory measurement of one sample of "I". The thermographs were obtained by measurement with the IR camera FLIR A615.

Table 6-3: Example of thermographs at the start and end of the by measurement with the infrared camera FLIR A615.



Here the area for the measurement as well as the point measurement (both marked red) can be seen. Only the temperature data of the point measurement were taken into consideration, the area measurement was dismissed because of a high similarity. On the other

hand, the use of data from point measurement leads to a better comparison with the other measurement systems, since they also only have point measurement.

The temperature curves of each sample as well as the mean curve for “C” can be seen in **Figure 6-3** as an example.

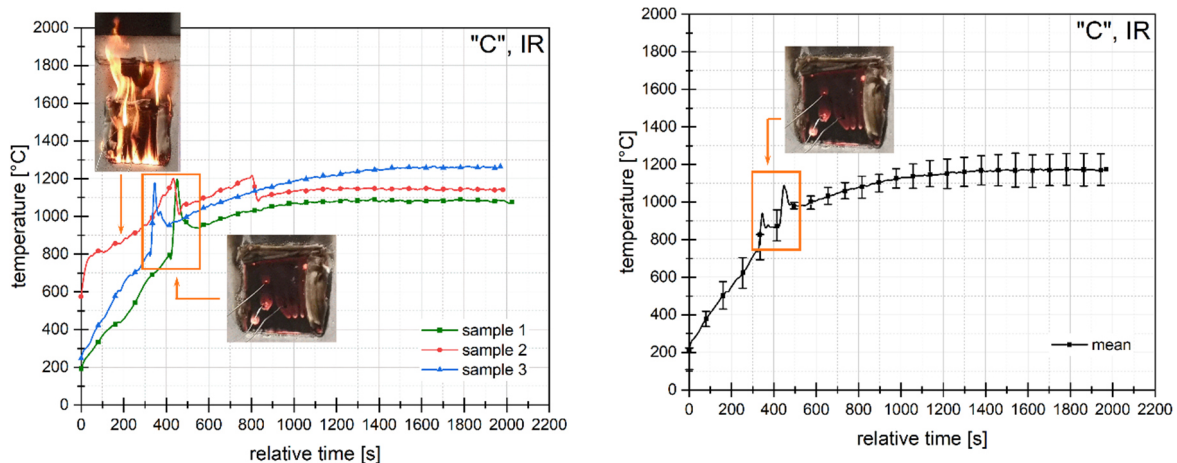


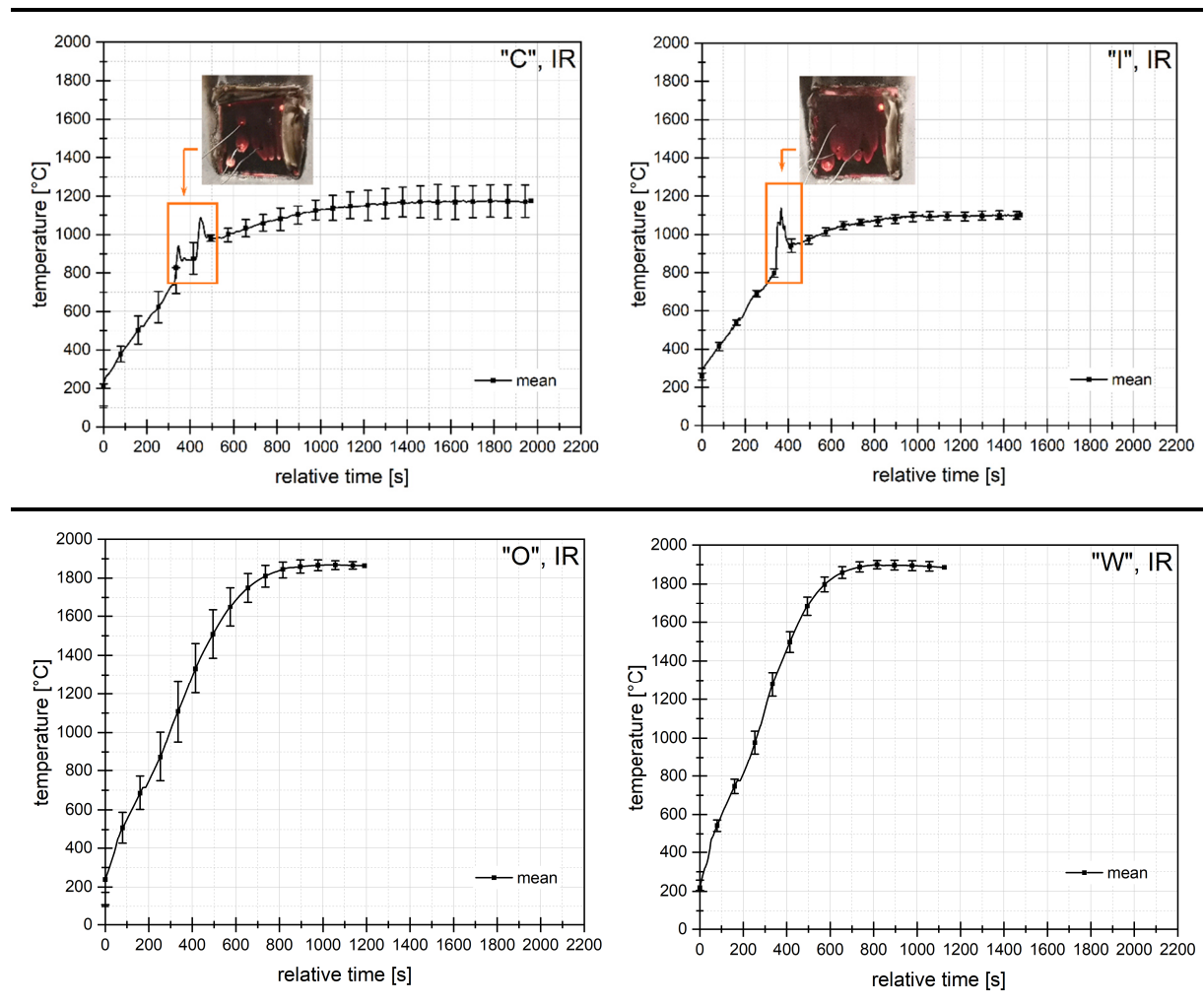
Figure 6-3: Left picture: temperature curves for each sample of “C”, right picture: mean temperature curve including standard deviation of “C”, obtained by IR camera

To calculate the mean temperature curve sample 2 was excluded because this sample started to burn immediately after it was inserted into the refractory frame. This can also be seen in the left picture of **Figure 6-3** (red curve). Furthermore, a peak in the temperature can be seen at the temperature curves of all three samples, more or less in the same time period. This is because the insulation always did catch fire for a short period of time, which can also be seen in both pictures of **Figure 6-3** (orange marked area).

In **Table 6-4** the mean temperature curves of all four cases including standard deviation are shown. The scale is purposely the same for all diagrams to ensure a good and easy comparability of the curves. The temperature curves for the individual samples can be found in the appendix, **Chapter B.1**.

For “I” again a peak in temperature is visible, which is due to the inflammation of the insulation. If the mean values of “I” and “W” are taken into consideration, it can be stated that the standard deviation is at a very low level. For “O” the standard deviation is a bit higher, but at the end temperature it is again very low. This is due to the fact, that the temperature curve of sample 3 was shifted to higher temperatures compared to the other two samples (see also **Table B-2**, “O” in the appendix). A reason for these higher temperatures can be an insufficient insulation of the sample between the plate and the refractory frame.

Table 6-4: Mean temperature curves of all four cases including standard deviation, obtained by the infrared camera FLIR A615.



The summary of the mean temperature curves of all four cases is pictured in **Figure 6-4**.

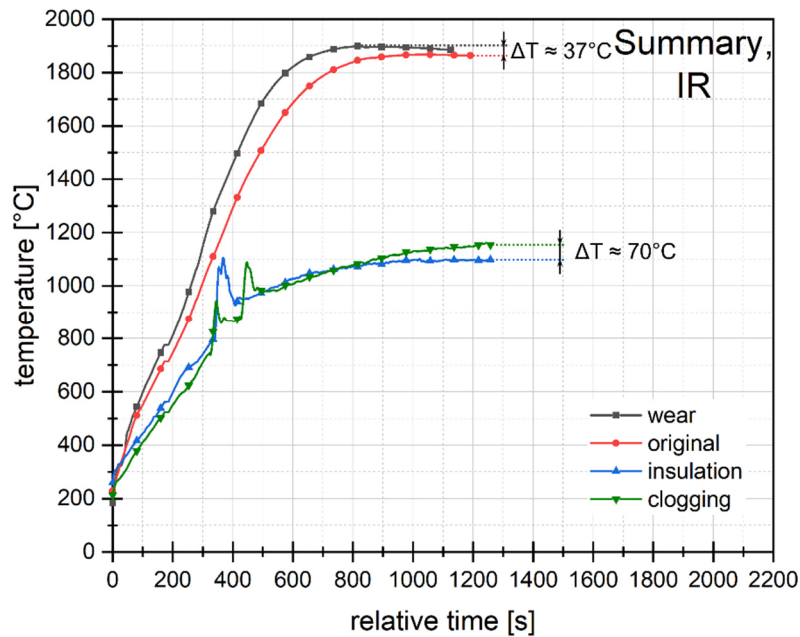


Figure 6-4: Summary of the mean temperature curves of all four cases, obtained by IR camera.

Here, a clear difference in the end temperatures can be seen. If “O” and “W” are taken into account, the temperature difference (ΔT) at the end is 37 °C. This leads to the assumption that the detection of wear could be possible if the end temperatures are considered. If “C” and “I” are compared, the end temperatures also show a difference ($\Delta T \approx 70$ °C), but not as expected. “I” shows a higher end temperature than “C”, which would have been expected to be vice versa. This can be explained by the high standard deviation of “C” (see also **Figure 6-3**).

Furthermore, a drop of the temperature is noticeable at the end of the mean temperature curve of “W”. This drop is also visible by measurement with the pyrometer and thermocouples (see also **Figure 6-5** and **Figure 6-8**). Since the measurement with thermocouples also shows this drop, optical effects can be excluded. Hence, this drop is most likely due to a higher heat removal on the surface of the sample. However, this should be examined in more detail in case this topic is pursued in future work.

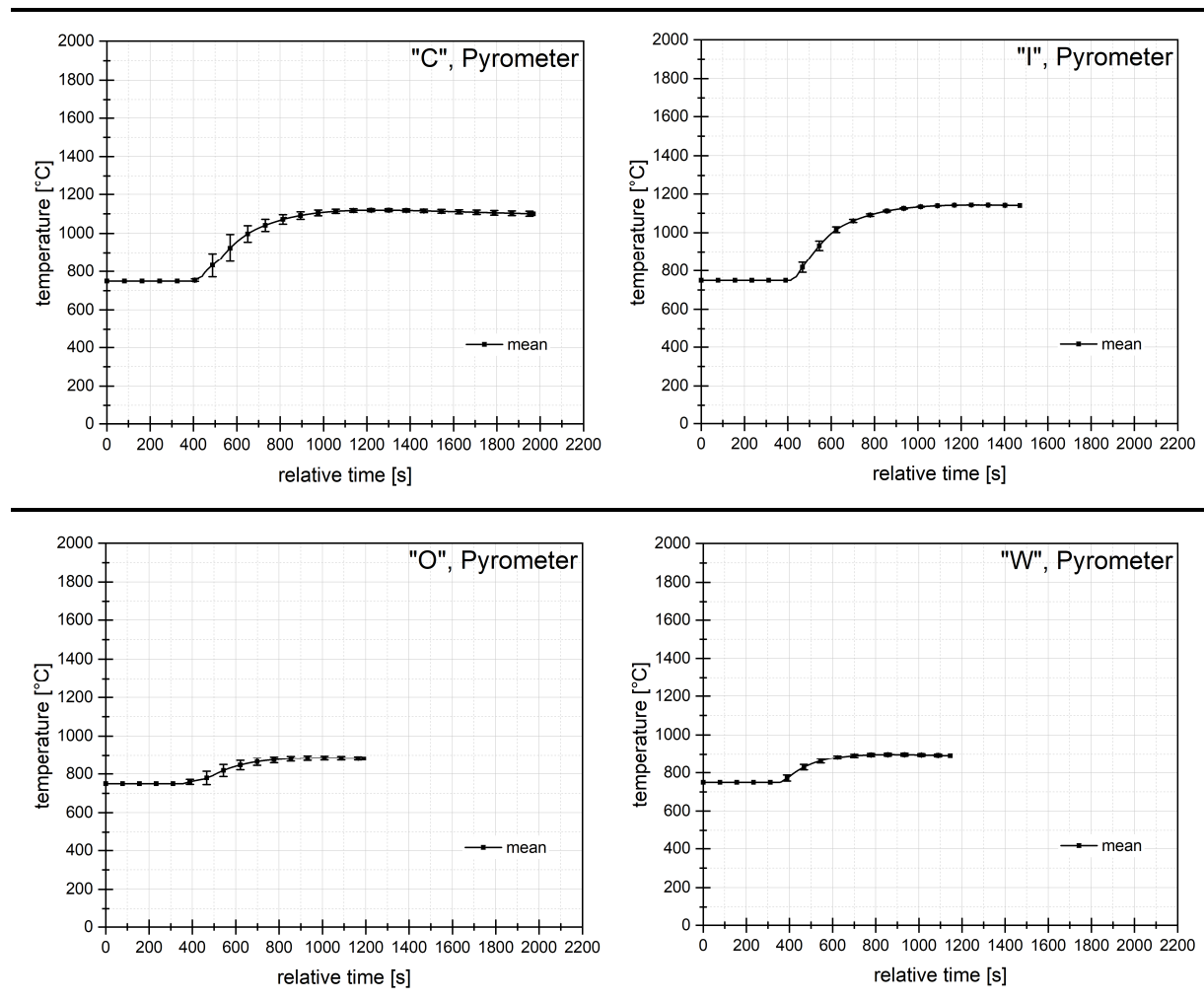
The relation of the end temperatures for the curves obtained by the measurement with the infrared camera is summarized using **Equation (6-1)**:

$$T_{"W", IR} > T_{"O", IR} > T_{"C", IR} > T_{"I", IR} \quad (6-1)$$

6.2.2 Pyrometer

The mean temperature curves including standard deviation, which were obtained using the pyrometer Metis M3 from Sensortherm, are shown in **Table 6-5**. It is remarkably that in approximately the first 400 seconds a constant temperature of 750 °C (the lower limit of the pyrometer) can be seen before it rises.

Table 6-5: Mean temperature curves of all four cases including standard deviation, obtained by the pyrometer Metis M3.



For the mean temperature curve of “C”, sample 2 was excluded because it started to burn almost immediately after inserting it into the furnace. The standard deviation of all curves is at a low level, indicating a good reproducibility. Furthermore, if these diagrams are compared to the ones obtained by the infrared camera (see **Figure 6-3** and **Table 6-4**), the temperature is lower. This is a result of the emissivity dependence of the measurement systems, which is different for the pyrometer and the IR camera.

In **Figure 6-5** the summary of the mean temperature curves of all cases can be seen. A more detailed diagram regarding the final temperature difference can be found in the appendix, **Chapter B.2**.

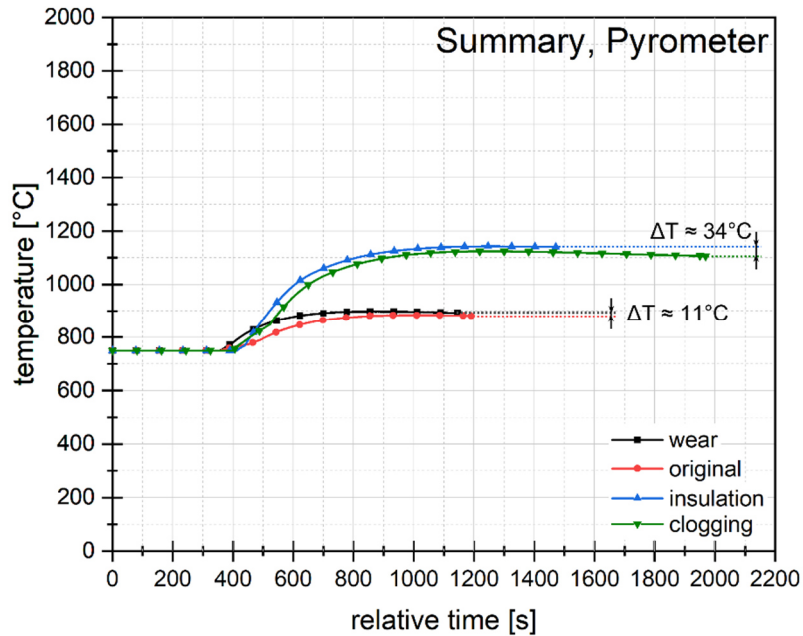


Figure 6-5: Summary of the mean temperature curves of all four cases, obtained by pyrometer.

What immediately stands out in this diagram is the fact that the insulated samples have a higher end temperature than those without insulation. This is most likely due to differences in the emissivity of the insulation material (white colour) and the ISO material (black colour). Comparing the red (“O”) and the black curve (“W”), a difference in the end temperature of around 11 °C can be observed. This can be additionally seen more detailed in **Figure B-1** in the appendix. The end temperatures are as expected, “W” shows a higher temperature as “O”. Also, between the green (“C”) and the blue (“I”) curve, a temperature difference at the end can be seen ($\Delta T \approx 34$ °C). The temperature curve of “C” shows a lower maximum than the curve of “I” which is as anticipated.

Equation (6-2) shows the summary of the end temperatures obtained with the help of the pyrometer:

$$T_{"I", \text{Pyr.}} > T_{"C", \text{Pyr.}} > T_{"W", \text{Pyr.}} > T_{"O", \text{Pyr.}} \quad (6-2)$$

6.2.3 BST

During the measurement with the BST some problems occurred. As the device is calibrated for temperatures above 1000 °C, some of the temperatures could not be recorded. Furthermore, the BST lost connection during the measurement of the samples of “C”. Thus, no data is available for this case. Due to the lack of data, the evaluation of the temperatures differs from the other devices. The results can be seen in **Figure 6-6**. Here, the temperature, the strength of the signal and the quality of the signal can be seen over time. Furthermore, the order of the testing procedure is shown here.

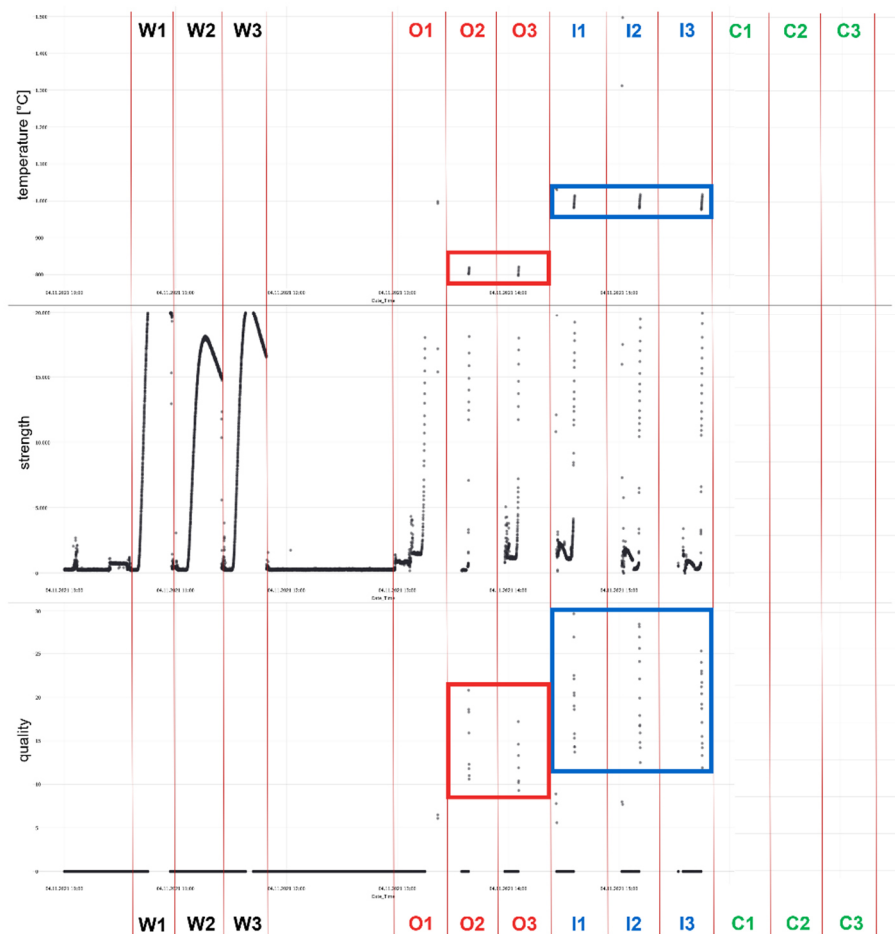


Figure 6-6: Results of the measurement with the BST.

For “W” (W1 – W3) the strength of the signal was rather high, but the signal quality too low to record any temperature. For “O” (O1 – O2) the quality of the signal was good enough to get at least some results. The temperature of sample 2 and 3 lies between 800 – 850 °C. The samples of “I” showed the best quality of the signal. Here, the temperature is again higher than for “O”, which can be explained by the difference in emissivity. Due to the lack of data, no

statement about the possibility of clogging or wear detection by temperature measurement with the use of the broadband spectral thermometer can be given.

The end temperatures of “I” and “O” of the measurement with the BST is expressed through **Equation (6-3)**:

$$T_{"I", \text{BST}} > T_{"O", \text{BST}} \quad (6-3)$$

6.2.4 Thermocouples

The samples were equipped with three thermocouples per sample acting as a reference temperature measurement. The positioning of the thermocouples can be seen in **Figure 5-3**. Additionally, one thermocouple was placed on the surface of the sample. During the testing procedure some of the thermocouples partially provided falsified values which are explained later within this chapter. The mean temperature curves of the thermocouples which were placed at the middle and near the hot face of the samples can be seen in **Figure B-2** and **Figure B-3** in the appendix. The measurement errors can most likely be explained due to interaction between the alloy of the thermocouples and the graphite inside the samples. Although the thermocouples were chosen correctly regarding the temperature range, it can be seen in **Figure 6-7**, that the tip of the thermocouples are partly melted or annealed. Thus, it happened that sometimes a piece of the thermocouples stayed inside the samples.

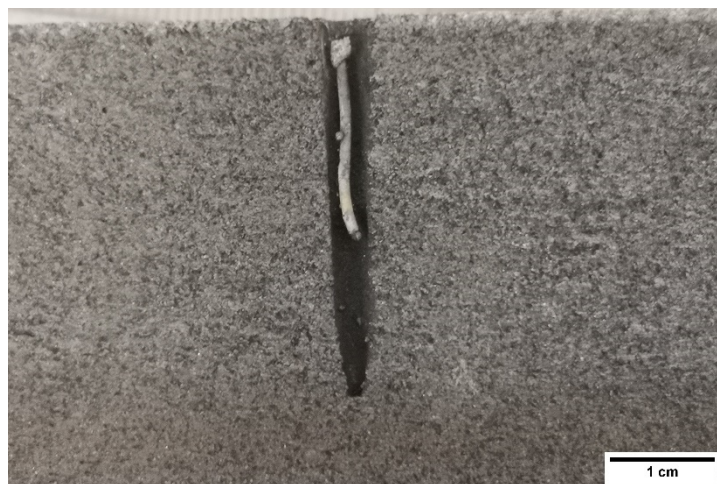
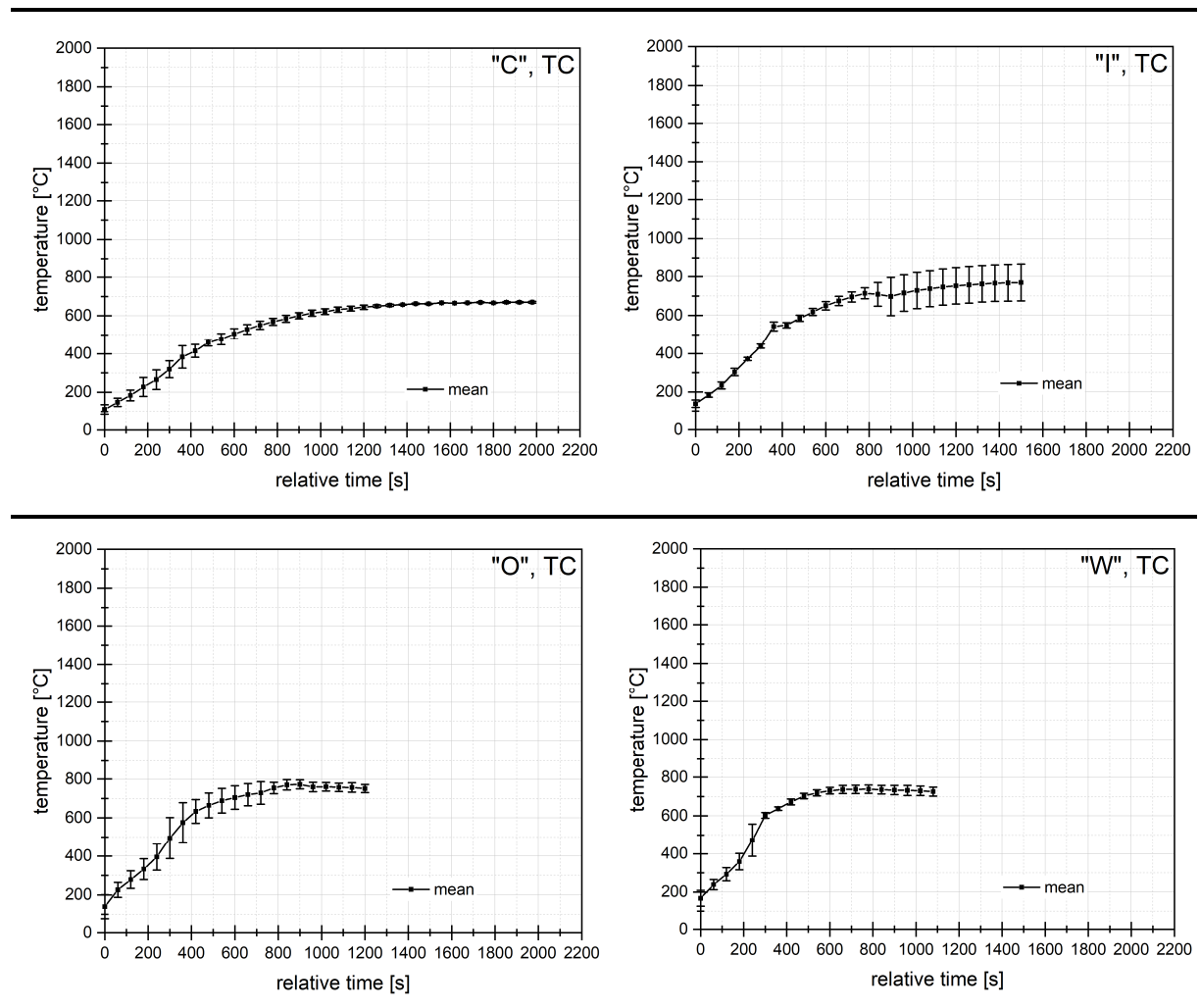


Figure 6-7: Broken tip of the thermocouple in a sample of “I”.

Only the thermocouples on the surface provided reliable and reproducible results. The mean temperature curves of the surface thermocouples can be seen in **Table 6-6**. More temperature curves for each sample can be found in the appendix, **Chapter B.3**.

Table 6-6: Mean temperature curves of all four cases including standard deviation, obtained by the surface thermocouples, type N.



To calculate the mean temperature curve of “C”, sample 2 was again excluded because it did not catch fire during heating up. The high standard deviation at the end of the temperature curve of “I” is a result of the attempt to change the placement of the thermocouple during measurement of sample 1. This was done, because the thermocouple poked through the insulation, resulting in the measurement of the higher temperature at the interface between the ISO material and the insulation, instead of the insulation surface temperature.

The summary of the mean temperature curves of all four cases is shown in **Figure 6-8**. The mean temperature curves in more detail are shown in **Figure B-4** in the appendix.

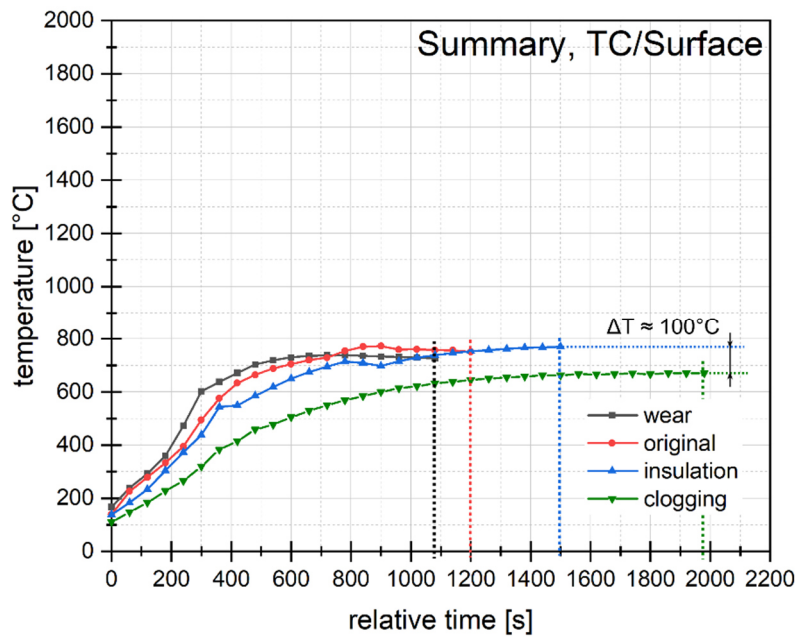


Figure 6-8: Summary of the mean temperature curves of all four cases, obtained by thermocouples.

By measurement with thermocouples, the difference in the end temperature between “C” and “I” can be seen most clearly ($\Delta T \approx 100\text{ }^{\circ}\text{C}$). On the other hand, there is no possibility to make a statement about the wear, if only the end temperature is taken into consideration. This is because the end temperature of “O” is higher than that of “W”, which is not as expected.

This can be summarized with **Equation (6-4)**:

$$T_{\text{“I”}, \text{TC}} > T_{\text{“O”}, \text{TC}} > T_{\text{“W”}, \text{TC}} > T_{\text{“C”}, \text{TC}} \quad (6-4)$$

Furthermore, in **Figure 6-8** the duration of the laboratory trials is clearly visible. It can be seen that the measurement of “C” took the longest time, followed by “I”, then “O”, and lastly “W” took the shortest time. These measuring times are as expected, since the thickness of the samples is reducing from “C” to “W” (also see **Figure 5-3**).

6.3 Comparison

In this chapter, the mean temperature curves of each measurement method are reviewed in more detail. “C” and “I” are compared to get a conclusion about clogging detection. The comparison of “O” and “W” should lead to a better understanding if and how wear can be detected. Therefore, the slopes of the temperature curves are compared to give a statement about the difference in heating rates for each case. This could only be done for the infrared

camera and the thermocouples. Because the pyrometer started the measurement above 750 °C, the heating rate cannot be observed. But if a closer look is taken on the starting point of the temperature curves, a similar trend can be detected.

6.3.1 Wear

To examine whether contactless temperature measurement is sufficient for wear detection, the slope of the mean temperature curves for “O” and “W” was calculated for the first 300 seconds. Therefore, a straight line was fitted, and the slope of this line was calculated. The results for the mean temperature curves obtained by infrared camera and thermocouples can be seen in **Table 6-7**.

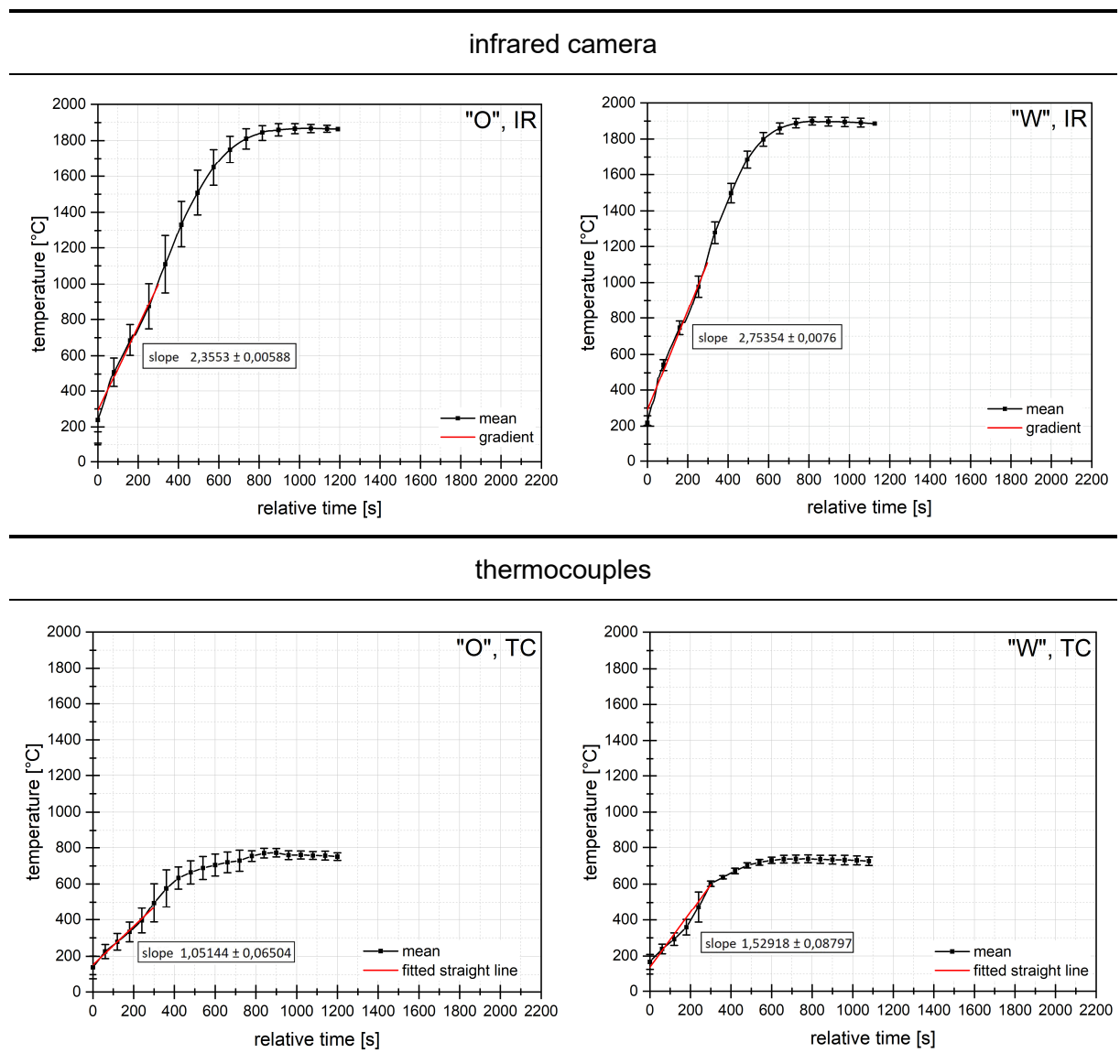
In case of the infrared camera, it can be seen that the slope for “O” is around 2.36, whereas the slope for “W” is approximately 2.75. This clearly indicates that the thinner sample of “W” has a higher heating rate compared to the sample of “O”. The curves obtained by the thermocouples show a similar picture. The slope of “O” is about 1.05, and the slope for “W” is approximately 1.53. This means, that a detection of wear is possibly doable if the heating rate is considered, by measurement with an IR camera. This is also verified by the measurement using thermocouples.

Equation (6-5) and **(6-6)** summarize the heating rates of “O” and “W”:

$$\text{slope}_{\text{W}, \text{IR}} > \text{slope}_{\text{O}, \text{IR}} > \text{slope}_{\text{W}, \text{TC}} > \text{slope}_{\text{O}, \text{TC}} \quad (6-5)$$

$$2.75 > 2.36 > 1.53 > 1.05 \quad (6-6)$$

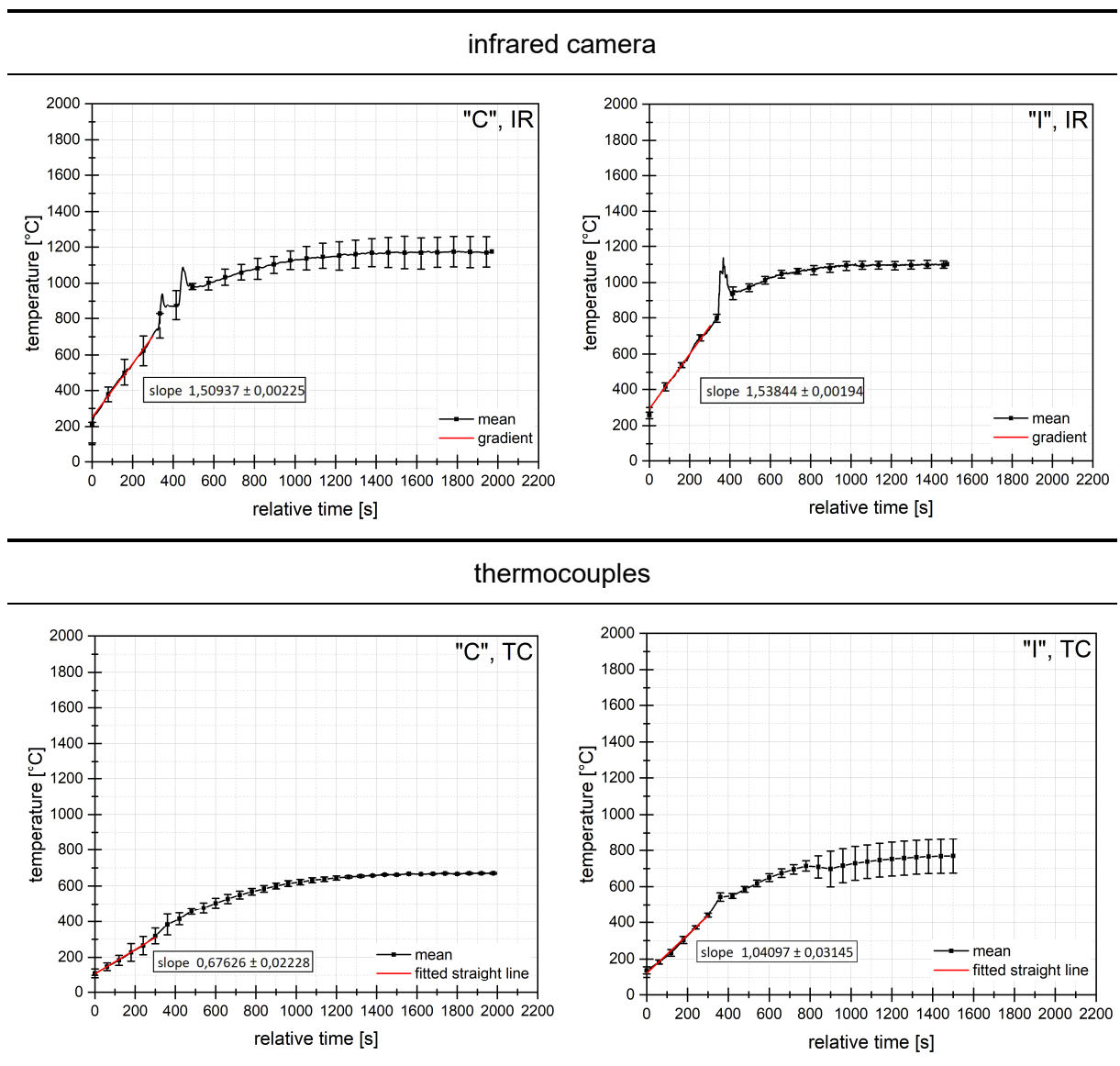
Table 6-7: Calculated heating rate (slope of a fitted straight line) for "O" and "W" on the mean temperature curves obtained by measurement with IR camera and thermocouples.



6.3.2 Clogging

For "C" and "I", the same procedure was done. A straight line was fitted in the area of the first 300 seconds to obtain the heating rate (slope of the straight line). The diagrams can be seen in **Table 6-8**.

Table 6-8: Calculated heating rate (slope of a fitted straight line) for “C” and “I” on the mean temperature curves obtained by measurement with infrared camera and thermocouples.



In case of the infrared camera, the difference of the heating rate of “C” and “I” is not as big as for “O” and “W”. But still, it can be seen that the heating rate of “I” is slightly higher (around 1.54) than for “C” (approximately 1.51). In case of the mean temperature curves obtained by thermocouples, the difference in the heating rate (slope of the fitted straight line) is also significant. For “C” the slope is about 0.68, whereas for “I” it is approximately 1.04. If the heating rate is taken into account, the detection of clogging via contactless temperature measurement is sufficient by using an infrared camera. The trend of the heating rate is also verified by the temperature curves obtained by thermocouples.

Equation (6-7) and (6-8) shows the relation of the heating rates of “C” and “I”:

$$\text{slope}_{"I", IR} > \text{slope}_{"C", IR} > \text{slope}_{"I", TC} > \text{slope}_{"C", TC} \quad (6-7)$$

$$1.54 > 1.51 > 1.04 > 0.68 \quad (6-8)$$

6.3.3 Pyrometer

A more detailed diagram of the mean temperature curves as well as the starting points of these curves obtained by measurement with the pyrometer can be seen in **Figure 6-9**. The starting points mark the points, where the temperature is above the measurement limit of 750 °C.

The first mean temperature curve, which reaches a temperature above 750 °C is "W" after approximately 356 seconds. This indicates the highest heating rate of the four cases, which is in good accordance with the heating rates observed by IR camera and thermocouples. The next one is the mean temperature curve of "O" at about 357 seconds, which is as expected. "C" and "I" show a different picture. Here the mean temperature curve of "C" starts first (after approximately 401 seconds), leading to the assumption that this curve has a higher heating rate than the curve of "I". The mean temperature curve of "I" starts at about 413 seconds, which is significantly later than in "C".

The starting times are summarized by **Equation (6-9)** and **(6-10)**.

$$t_{"W", Pyr.} > t_{"O", Pyr.} > t_{"C", Pyr.} > t_{"I", Pyr.} \quad (6-9)$$

$$356 \text{ s} > 357 \text{ s} > 401 \text{ s} > 413 \text{ s} \quad (6-10)$$

If these are compared with **Equation (6-5)**, **(6-6)**, **(6-7)** and **(6-8)** more or less the same tendency is noticeable. Only the starting times of "C" and "I" are vice versa compared to the heating rates. As can be seen in the upper diagram of **Figure 6-9**, however, this changes after the sharp bend of the mean temperature curve of "I".

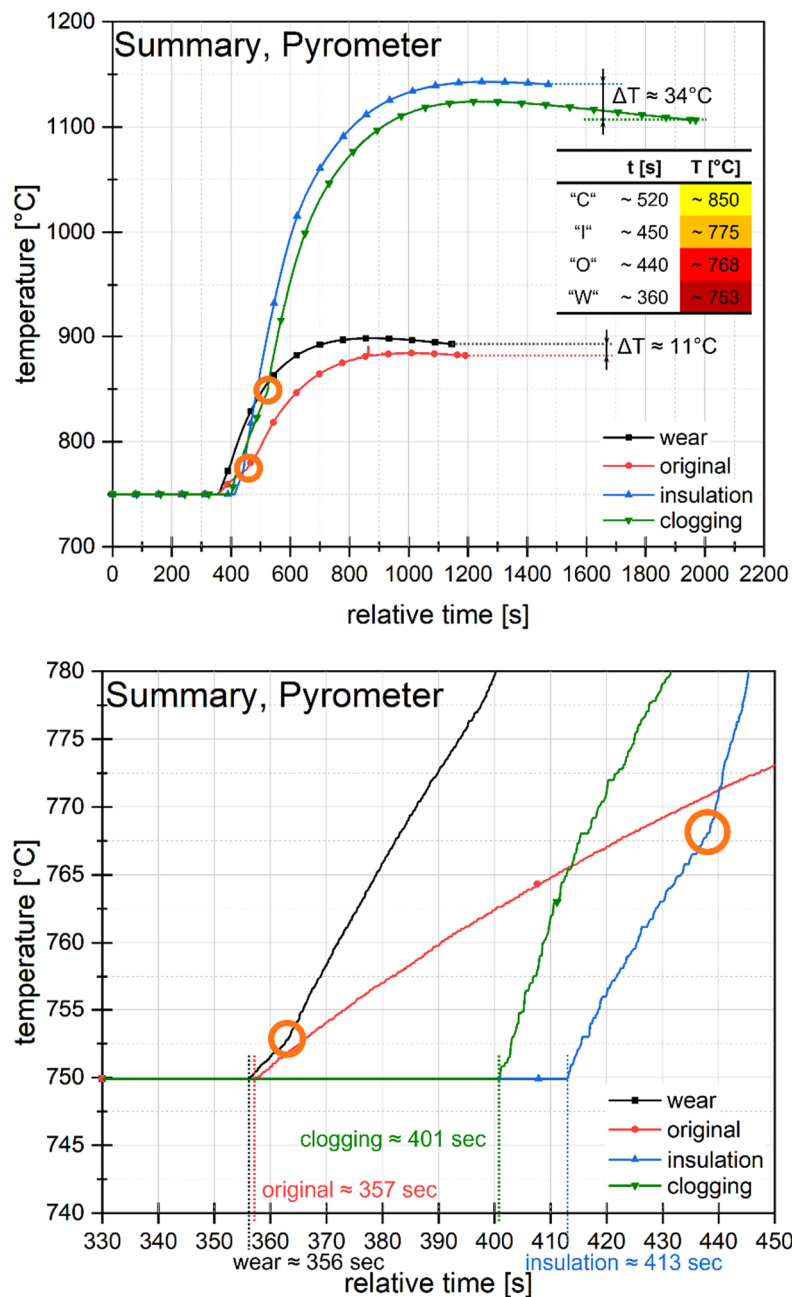


Figure 6-9: Upper diagram: more detailed diagram of the mean temperature curves of all four cases by measurement with the pyrometer. Lower diagram: detailed section of the starting points of the mean temperature curves.

Furthermore, as can be seen in both diagrams of **Figure 6-9**, each mean temperature curve shows a sharp bend (orange marked areas). If the curves of "O" and "W" are inspected in more detail, these curves show a similar slope before as well as after the sharp bend. The same is true for the curves of "C" and "I". Only the sharp bends are occurring at different times and temperatures (also see the table in the upper diagram of **Figure 6-9**). The temperatures as well as the times of the sharp bends show the same trend. In case of the temperature curve of

“C” the bend occurs at the highest temperature and the latest time, whereas the curve of “W” bends at the lowest temperature but the earliest time. This is in good accordance with the fact that “W” is the thinnest sample and “C” the thickest (see also **Figure 5-3**). This leads to the assumption that the sharp bend comes from some changes inside the refractory material, which leads to changes of the heat transfer coefficient.

7 Summary and outlook

In the course of this thesis, the question whether contactless temperature measurement is sufficient for clogging and refractory wear detection should be answered. Therefore, a comprehensive literature study regarding refractory topics, clogging, and temperature measurement methods was conducted. Furthermore, a laboratory test set-up was developed, to perform temperature measurements at typical operating temperatures. For this laboratory test samples were manufactured, which should reproduce four different cases: a clogged submerged entry nozzle, an un-clogged submerged entry nozzle, an unused ladle shroud, and a worn ladle shroud. For the measurement three different contactless temperature measurement methods were used. These are the infrared camera FLIR A615, the two-colour pyrometer Metis M3 from Sensortherm and the broadband spectral thermometer. As a reference also thermocouples type N and S were used to measure the temperature at three different spots of the samples. To verify if a detection of clogging and refractory wear is possible in principle, the end temperature of the obtained temperature curves, as well as the heating rate were examined.

A general outcome of the trial procedure and the measurement results can be summarized as follows:

- the laboratory trial set-up worked well, even without the incorporation of liquid steel,
- measurement with thermocouples were sufficient as a reference,
- the contactless temperature measurement devices show significant differences regarding the type of material (black ISO material vs. white insulating material),
- for further trials it is recommended to
 - optimize the trial set-up,
 - rethink the selection and design of the thermocouples,

- the way of placing the thermocouples like using a ceramic protection capillary to avoid the diffusion of carbon, as well as
- have a further look into contactless temperature measurement devices regarding emissivity and other calibration parameters

The results showed that the detection of both, clogging and wear, is possible in a laboratory scale. This is true if the end temperatures are taken into consideration as well as in case of the heating rates. If Clogging (“C”) and Insulation (“I”) are compared, the end temperature of the samples of “I” is higher than the end temperature of “C” for the pyrometer and the thermocouples. By the use of the IR camera this is vice versa, in case of the BST no data for “C” is available.

For the comparison of Original (“O”) and Wear (“W”), a similar picture can be seen. In case of the infrared camera and the pyrometer the end temperature of “W” is higher than of “O”, which is as expected. Just the temperatures obtained by measurement with thermocouples show different results. Here the end temperature of “O” is higher than the end temperature of “W”. If the measurements with the BST are taken into consideration, again a statement is not possible since no data for “W” is available.

The evaluation of the heating rates (slopes) for two different measurement systems, IR camera and thermocouples, show that the heating rate of “I” is higher than “C” with both measurement devices. Just like the heating rate of “W” is higher than the heating rate of “O”. All these findings are summarized in **Table 7-1**, including a colour code. Bright yellow indicates the highest end temperature (T_{end}), the fastest heating rate ($\Delta T/\Delta t$) as well as the lowest starting time (t_{start}). The darker the colour gets, the lower the temperature, the slower the heating rate and the longer the starting time.

Table 7-1: Summary of the outcome of this thesis.

case	IR camera		Pyrometer		BST	Thermocouples	
	T_{end}	$\Delta T/\Delta t$	T_{end}	t_{start}	T_{end}	T_{end}	$\Delta T/\Delta t$
“C”	1.160 °C	1,51 °C/s	1.106 °C	401 s	-	670 °C	0,68 °C/s
“I”	1.099 °C	1,54 °C/s	1.140 °C	413 s	1.030 °C	770 °C	1,04 °C/s
“O”	1.864 °C	2,36 °C/s	882 °C	357 s	850 °C	751 °C	1,05 °C/s
“W”	1.885 °C	2,75 °C/s	893 °C	356 s	-	725 °C	1,53 °C/s

The best results in case of the contactless temperature measurement systems were obtained using the pyrometer. Here, the mean temperature curves are as expected, showing quite remarkable differences in the end temperature for each case. The only discrepancy is the fact, that the samples with insulations (“C” and “I”) show higher temperatures than the ones without insulation (“O” and “W”). The BST did not work as expected, which is most likely due to the lack of a new calibration for lower temperatures and the system still in a development stage. The calibration of the BST for lower temperatures was not possible prior to this thesis because of a damaged calibration furnace.

During the laboratory trials some problems in case of the thermocouples were noticeable. The placement of the thermocouples inside the drilled holes of the sample was not controllable in a sufficient way during sample placement. It could not be ensured, that the thermocouples are always placed in the defined same depth. If future trials should be conducted, it should be taken care that the thermocouples are fixed inside the samples before inserting them into the furnace. Furthermore, the carbon inside the refractory material disturbed the measurement and seems to damage the thermocouples. Thus, it would be recommended to isolate the thermocouples from the surrounding refractory material if such trials are repeated. Also, the calibration and handling of the contactless temperature measurement devices must be taken care of in more detail. It would be recommended to consult an expert regarding contactless temperature measurement.

If this topic is pursued in further work, enhanced laboratory trials or field tests should be carried out to clarify whether it is possible to detect clogging and wear even if these phenomena only occur locally.

List of References

- [1] T. Vert, Refractory material selection for steelmaking (2016), John Wiley & Sons, Inc.
- [2] G. Routschka and H. Wuthnow, Handbook of Refractory Materials: Design - Properties - Testing. 4th edition (2012), Vulkan-Verlag GmbH.
- [3] K.G. Rackers, Mechanism and mitigation of clogging in continuous casting nozzles. Master Thesis, Illinois (1995).
- [4] H. Dösinger, C. McFarlane, G. Nitzl, Y. Tang and G. Hackl, Anticlogging Solutions for Isostatically Pressed Submerged Nozzles. RHI Bulletin (2015), 1, pp. 84–87.
- [5] J. Zhang, Q. Liu, S. Yang, Z. Chen, J. Li and Z. Jiang, Advances in Ladle Shroud as A Functional Device in Tundish Metallurgy: A Review. ISIJ Int. 59 (2019), 7, pp. 1167–1177.
- [6] P. Colucci, F. Leclercq, D. Verrelle, E. Iida and M. Nakamura, Improvement of metallurgical qualities of fluorine steels by the use of mogul submerged entry nozzles. European Conference on Continuous Casting (ECCC), Riccione, Italy (2008).
- [7] T. Matsunaga, M. Ogata, M. Nakamura and E. Iida, Practical use of mogul shaped submerged entry nozzle at chubu steel plant. European Conference on Continuous Casting (ECCC), Riccione, Italy (2008).
- [8] S. Devic and M. Cocic, Submerged entry Nozzles based on alumina-graphite refractory material in the process of continuous steel casting 58 (2017), 2, pp. 151–157.
- [9] S. Devic and L. Marceta, Microscopic analysis of alumina-graphite SEN external deposit. European Conference on Continuous Casting (ECCC), Riccione, Italy (2008).

- [10] V. Kircher, Burhanuddin and H. Harmuth, Design, operation and evaluation of an improved refractory wear testing technique. *Measurement* 178 (2021), pp. 109429.
- [11] C. Capurro, C. Cicutti, P. Galliano, F. Fuhr, G. Torga and J. Scoccia, Optimization of submerged entry nozzles wearing. *European Conference on Continuous Casting (ECCC)*, Riccione, Italy (2008).
- [12] B.M. Thethwayo and J.D. Steenkamp, A review of carbon-based refractory materials and their applications. *J. S. Afr. Inst. Min. Metall.* 120 (2020), 11
- [13] K.G. Rackers and B.G. Thomas, Clogging in Continuous Casting Nozzles. 78th *Steelmaking Conference Proceedings* (1995), Vol. 78, pp. 73–734.
- [14] B.G. Thomas and H. Bai, Tundish nozzle clogging - application of computational models. 18rd *Process Technology Division Conference Proceedings* (2001), Vol. 18
- [15] H. Bai and B.G. Thomas, Effects of Clogging, Argon Injection, and Continuous Casting Conditions on Flow and Air Aspiration in Submerged Entry Nozzles. *Metallurgical and Materials Transactions B* (2001), Volume 32B, pp. 707–722.
- [16] L. Zhang and B.G. Thomas, Inclusions in continuous casting of steel. *XXIV National Steelmaking Symposium*, Morelia, Mich, Mexico (2003), pp. 138–183.
- [17] S. Basu, S.K. Choudhary and N.U. Girase, Nozzle Clogging Behaviour of Ti-bearing Al-killed Ultra Low Carbon Steel. *ISIJ International* (2004), Vol. 44, pp. 1653–1660.
- [18] N.U. Girase, S. Basu and S.K. Choudhary, Development of indices for quantification of nozzle clogging during continuous slab casting. *Ironmaking & Steelmaking* 34 (2007), 6, pp. 506–512.
- [19] A. Dey and R. Thackray, A study of the interactions of exogenous inclusions with SEN walls during continuous casting. *European Conference on Continuous Casting (ECCC)*, Riccione, Italy (2008).
- [20] S.-M. Cho, S.-H. Kim, R. Chaudhary, B.G. Thomas, H.-J. Shin, W.-R. Choi and S.-K. Kim, Effect of Nozzle Clogging on Surface Flow and Vortex Formation in the Continuous Casting Mold. *AISTech* (2011)
- [21] Z. Deng, M. Zhu, Y. Zhou and Du Sichen, Attachment of Alumina on the Wall of Submerged Entry Nozzle During Continuous Casting of Al-Killed Steel. *Metall and Materi Trans B* 47 (2016), 3, pp. 2015–2025.
- [22] J. Poirier, A review: influence of refractories on steel quality. *Metall. Res. Technol.* 112 (2015), 4, pp. 410.

- [23] J. Poirier, B. Thillou, M. Guiban and G. Provost, Mechanisms and countermeasures of alumina clogging in submerged nozzles. *Steelmaking Conference Proceedings* (1995), 451 - 456.
- [24] N. Sutcliffe, Slag/refractory and metal/refractory interactions during the production of stainless steels. VII International Conference on Molten Slags Fluxes and Salts (2004), pp. 423–436.
- [25] K. Goto, K. Kohno, T. Ikemoto, S. Hanagiri and T. Matsui, Progress and Perspective of Refractory Technology. *Nippon Steel Technical Report* (2013), No. 104
- [26] J. Ikäheimonen, K. Leiviskä, J. Ruuska and J. Matkala, Clogging prediction in continuous casting of steel. 15th Triennial World Congress, Barcelona, Spain (2002), pp. 143–147.
- [27] B. Trummer, W. Fellner, A. Viertauer, L. Kneis and G. Hackl, Purging Plugs for Soft Gas Bubbling: A Water Modelling Comparison of Hybrid and Slot Designs. *RHI Bulletin* (2014), 1, pp. 29–33.
- [28] B. Trummer, W. Fellner, A. Viertauer, L. Kneis and G. Hackl, A Water Modelling Comparison of Hybrid Plug, Slot Plug and Porous Plug Designs. *RHI Bulletin* (2016), 1, pp. 35–38.
- [29] N. Verma, P.C. Pistorius, R.J. Fruehan, M. Potter, M. Lind and S.R. Story, Transient Inclusion Evolution During Modification of Alumina Inclusions by Calcium in Liquid Steel: Part II. Results and Discussion. *Metall and Materi Trans B* 42 (2011), 4, pp. 720–729.
doi:10.1007/s11663-011-9517-2
- [30] R. Heinke and K. Takahama, Kinetic model for the formation of CaO and CaS in aluminum deoxidized steels by calcium treatment. *steel research* (1987), 58, No. 4, 162 - 166.
- [31] L. Holappa, Inclusion control for castability of resulphurized steels. *Steelmaking Conference Proceedings* (2001), 765 - 777.
- [32] R.B. Tuttle, J.D. Smith and K.D. Peaslee, Casting Simulation of Calcium Titanate and Calcium Zirconate Nozzles for Continuous Casting of Aluminum-Killed Steels. *Metall and Materi Trans B* 38 (2007), 1, pp. 101–108.
- [33] S. Abdelaziz, G. Megahed, I. El-Mahallawi and H. Ahmed, Control of Ca addition for improved cleanliness of low C, Al killed steel. *Ironmaking & Steelmaking* 36 (2009), 6, pp. 432–441.
- [34] S. Abraham, R. Bodnar, J. Raines and Y. Wang, Inclusion engineering and metallurgy of calcium treatment. *J. Iron Steel Res. Int.* 25 (2018), 2, pp. 133–145.

- [35] S. Zhou, Study of the clogging of the submersible nozzle in the continuous casting of stainless steel RE-253MA. *Metallurgist* (2013), Vol. 57, Nos. 5–6, pp. 510–515.
- [36] X. Han, K. Huan and S. Sheng, Performance evaluation and optimization design of photoelectric pyrometer detection optical system. *Defence Technology* 16 (2020), 2, pp. 401–407.
- [37] P. Smorscek, M.J. Wandelt and F. Liebelt, *Infrarotkameras in der Automobilindustrie* 2008, Nr. 3, pp. 46–49.
- [38] P. Conradie, G. Oosthuizen, N. Treurnicht and A. Al Shaalane, Overview of work piece temperature measurement techniques for machining of Ti6Al4V. *South African Journal of Industrial Engineering* (2012), Vol 23 (2), pp. 116–130.
- [39] J. Hartmann, New Developments in High-Temperature Measurement Techniques. *International Journal of Electrical and Computer Engineering Systems* (2014), Volume 5, Number 2
- [40] S.Y. Beck, Entwicklung eines Laborversuchs zur Vermessung unterschiedlicher Wandaufbauten hinsichtlich ihres Wärmedurchgangs mit Hilfe einer Wärmebildkamera. *Wissenschaftliche Arbeit, Tübingen* (2015).
- [41] R. Usamentiaga, P. Venegas, J. Guerediaga, L. Vega, J. Molleda and F.G. Bulnes, Infrared thermography for temperature measurement and non-destructive testing. *Sensors (Basel, Switzerland)* 14 (2014), 7, pp. 12305–12348.
- [42] M. Piasecka, D. Michalski and K. Strąk, Comparison of two methods for contactless surface temperature measurement. *EPJ Web Conf.* 114 (2016), pp. 2094.
- [43] D. Pan, Z. Jiang, Z. Chen, W. Gui, Y. Xie and C. Yang, Temperature Measurement Method for Blast Furnace Molten Iron Based on Infrared Thermography and Temperature Reduction Model. *Sensors (Basel, Switzerland)* 18 (2018), 11
- [44] J. Maron, Selecting non contact pyrometers & infrared thermometers. *Process Heating*
- [45] OPTRIS GmbH, Basic principles of non-contact temperature measurement.
- [46] Raytek Corporation, The principles of noncontact temperature measurement.
- [47] M.A. Khan, C. Allemand and T.W. Eagar, Noncontact temperature measurement. I. Interpolation based techniques. *Review of Scientific Instruments* (1991), 62 (2), pp. 392–402.
- [48] B. Müller and U. Renz, Development of a fast fiber-optic two-color pyrometer for the temperature measurement of surfaces with varying emissivities. *Review of Scientific Instruments* 72 (2001), 8, pp. 3366–3374.

- [49] J. Hartmann, High-temperature measurement techniques for the application in photometry, radiometry and thermometry. *Physics Reports* 469 (2009), 5-6, pp. 205–269.
- [50] A. Hug, Thermodynamische Eigenschaften von schwerionengeheizten hochschmelzenden Metallen. Dissertation, Darmstadt (2011).
- [51] E.M. Vuelban, F. Girard, M. Battuello, P. Nemeček, M. Maniur, P. Pavlásek and T. Paans, Radiometric Techniques for Emissivity and Temperature Measurements for Industrial Applications. *Int J Thermophys* 36 (2015), 7, pp. 1545–1568.
- [52] A. Tapetado, J. Diaz-Alvarez, M.H. Miguelez and C. Vazquez, Two-Color Pyrometer for Process Temperature Measurement During Machining. *J. Lightwave Technol.* 34 (2016), 4, pp. 1380–1386.
- [53] W. Devesse, D. de Baere and P. Guillaume, High Resolution Temperature Measurement of Liquid Stainless Steel Using Hyperspectral Imaging. *Sensors (Basel, Switzerland)* 17 (2017), 1
- [54] J. Zhao, Z. Liu, B. Wang, Y. Hua and Q. Wang, Cutting temperature measurement using an improved two-color infrared thermometer in turning Inconel 718 with whisker-reinforced ceramic tools. *Ceramics International* 44 (2018), 15, pp. 19002–19007.
- [55] P. Saunders, On the effects of temperature dependence of spectral emissivity in industrial radiation thermometry. *High Temp.-High Press.* 33 (2001), 5, pp. 599–610.
- [56] T. Karadzhev, D. Pulov and N. Angelov, Contactless measuring of temperature with differential photo receiver. *ETR* 3 (2019), pp. 101–104.
- [57] T. Larrick, Understanding modern infrared pyrometers for demanding steel mill applications.
- [58] RHI Magnesita GmbH, Broadband spectral thermometer (BST) (2020).
- [59] D. Ng and G. Fralick, Use of a multiwavelength pyrometer in several elevated temperature aerospace applications. *Review of Scientific Instruments* 72 (2001), 2, pp. 1522.
- [60] D. Michalski, K. Strąk and M. Piasecka, Comparison of two surface temperature measurement using thermocouples and infrared camera. *EPJ Web Conf.* 143 (2017), pp. 2075.
- [61] P.H. Westebbe, Untersuchungen an Kunst- und Kulturgut mittels der Infrarot-Thermografie: Eine zerstörungsfreie Analysemethode. Diplomarbeit, München (2004).
- [62] P.R.N. Childs, J.R. Greenwood and C.A. Long, Review of temperature measurement. *Review of Scientific Instruments* Volume 71 (2000), No 8, pp. 2959–2978.

[63] DIAS Infrared GmbH, Wärmebildkameras. <https://www.dias-infrared.de/waermebildkameras>, Accessed: 15.01.2022

[64] A.H. Khalid and K. Kontis, Thermographic Phosphors for High Temperature Measurements: Principles, Current State of the Art and Recent Applications. *Sensors* (Basel, Switzerland) 8 (2008), 9, pp. 5673–5744.

[65] FLIR, A615.

[http://www.thermokameras.com/Bedienungsanleitungen%20+%20Software/A-Serie/FLIR%20A615%20\(640x480%20Pixel\)%2025%20Grad%20Normalobjektiv.pdf](http://www.thermokameras.com/Bedienungsanleitungen%20+%20Software/A-Serie/FLIR%20A615%20(640x480%20Pixel)%2025%20Grad%20Normalobjektiv.pdf), Accessed: 15.01.2022

[66] Sensortherm, Metis M3.

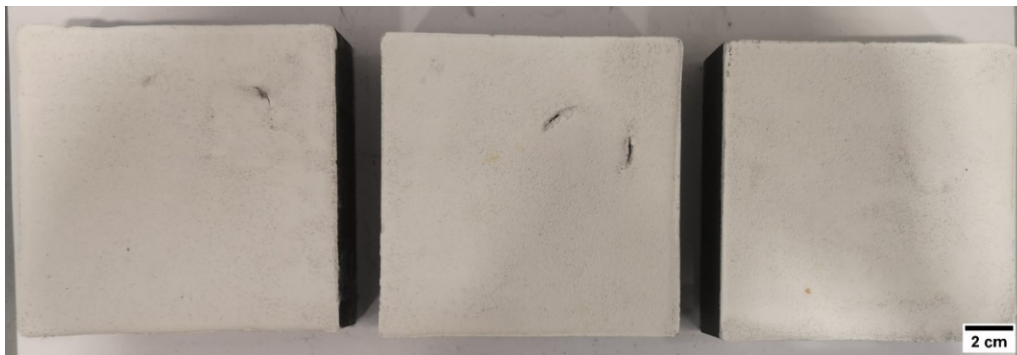
https://www.sensortherm.de/userfiles/file/datenblaetter/en/Sensortherm-Datasheet_Metis_M3-Series.pdf, Accessed: 15.01.2022

A. Physical sample analysis

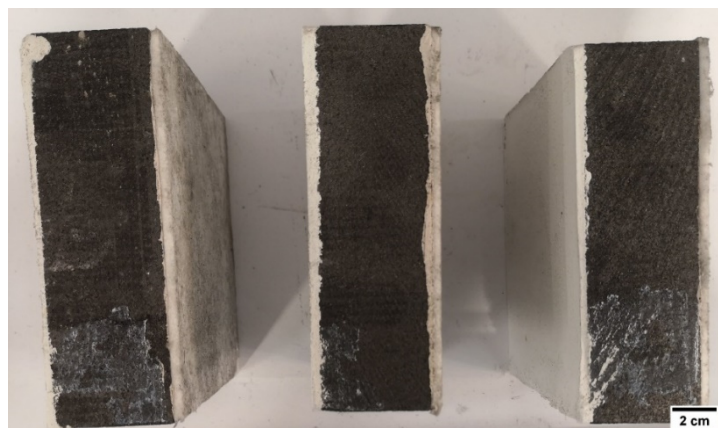
In this chapter the remaining pictures of the samples are shown. In **Table A-1** the samples of Clogging (“C”) can be seen.

Table A-1: Overview of the samples of “C” before and after the laboratory trials.

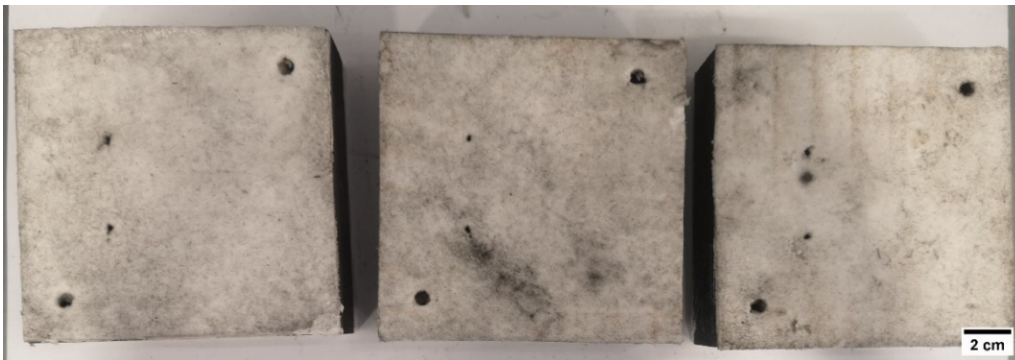
Hot face, before trial



Side face, before trial



Cold face, before trial



Cold face, after trial



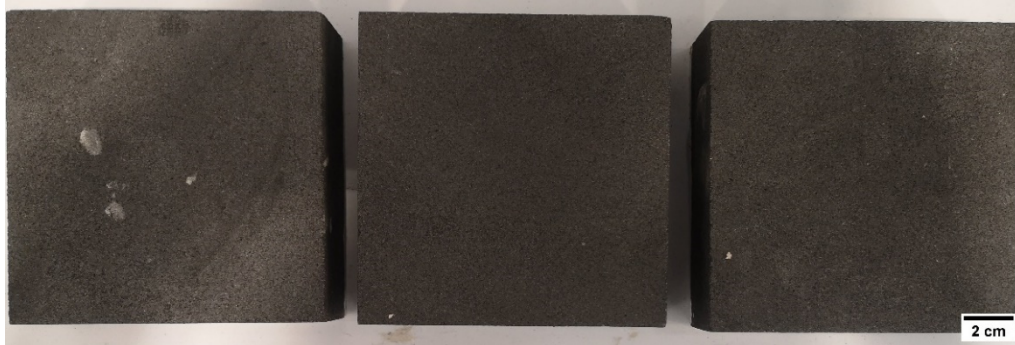
Hot face, after trial



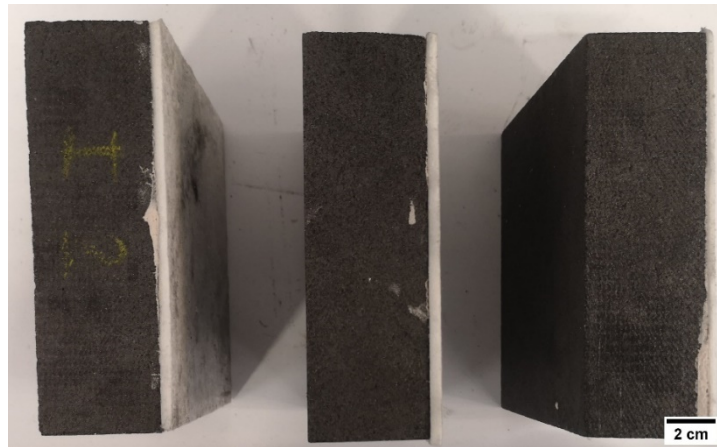
Table A-2 shows the samples of Insulation ("I").

Table A-2: Overview of the samples of "I" before and after the laboratory trials.

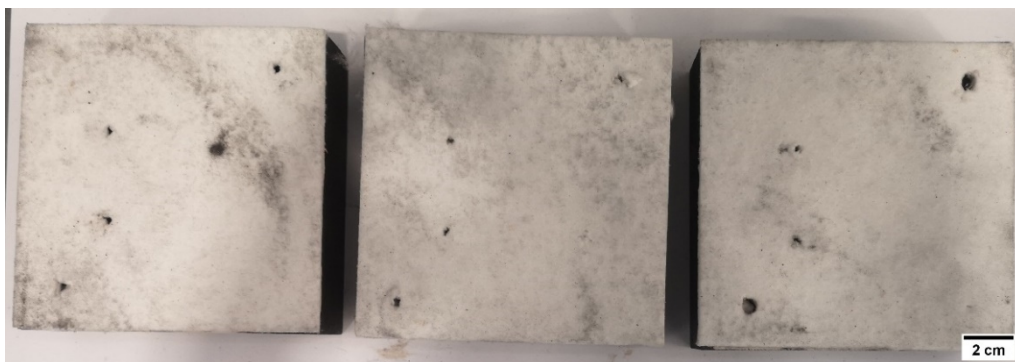
Hot face, before trial



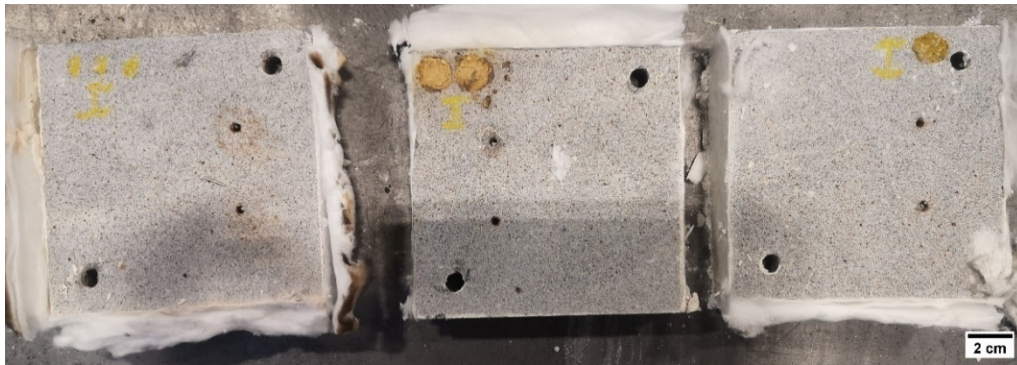
Side face, before trial



Cold face, before trial



Cold face, after trial, without insulation



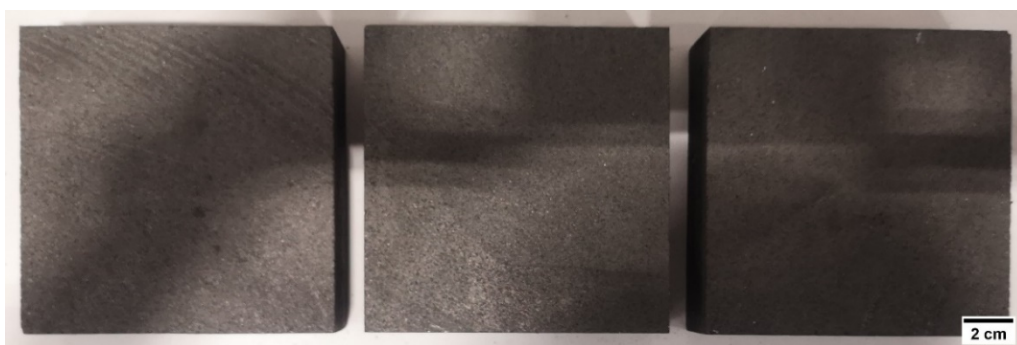
Cold face, after trial, with loose insulation



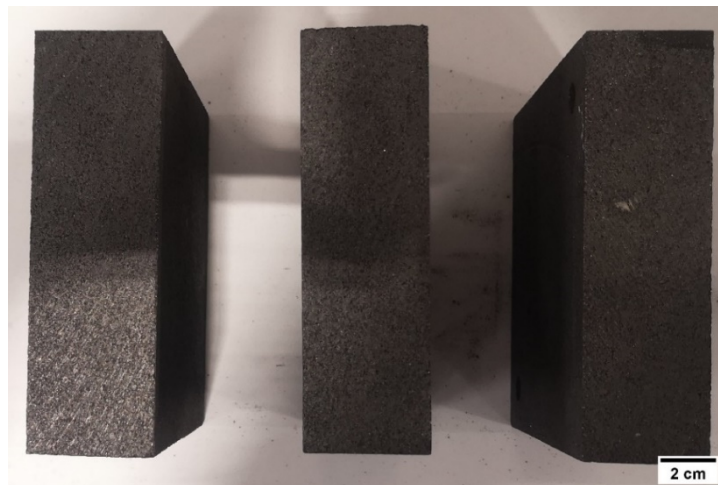
The samples of Original (“O”) can be seen in **Table A-3**

Table A-3: Overview of the samples of “O” before and after the laboratory trials.

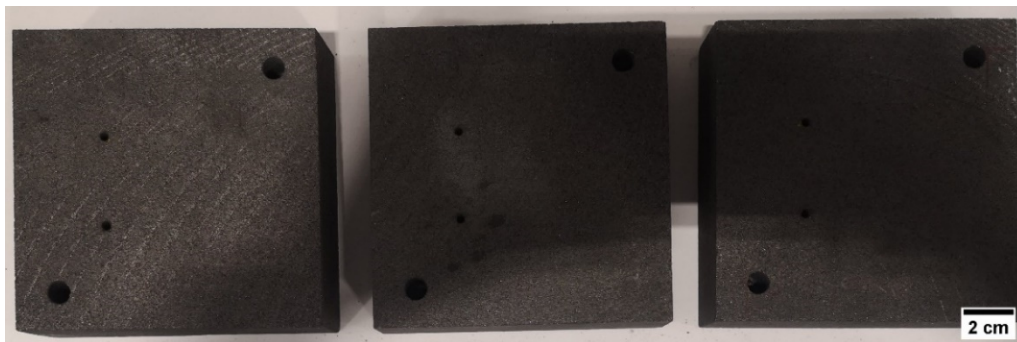
Hot face, before trial



Side face, before trial



Cold face, before trial



Cold face, after trial, without insulation



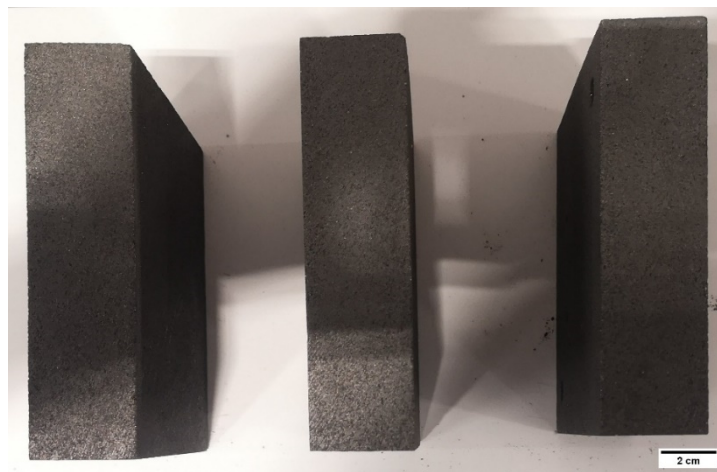
Finally, **Table A-4** shows the samples of Wear (“W”).

Table A-4: Overview of the samples of “W” before and after the laboratory trials.

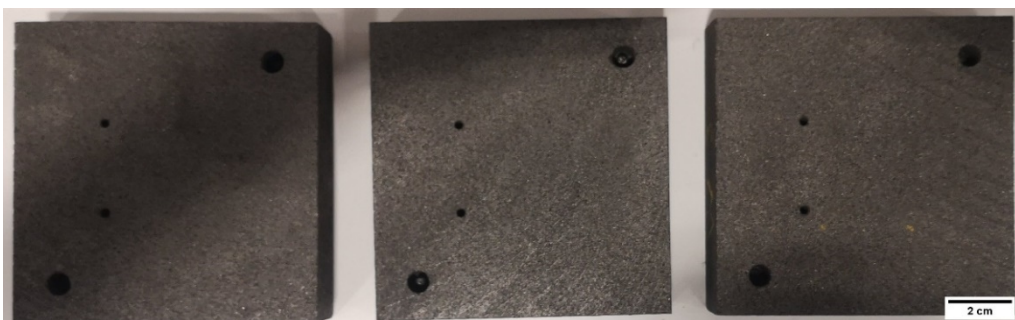
Hot face, before trial



Side face, before trial



Cold face, before trial



Cold face, after trial, without insulation

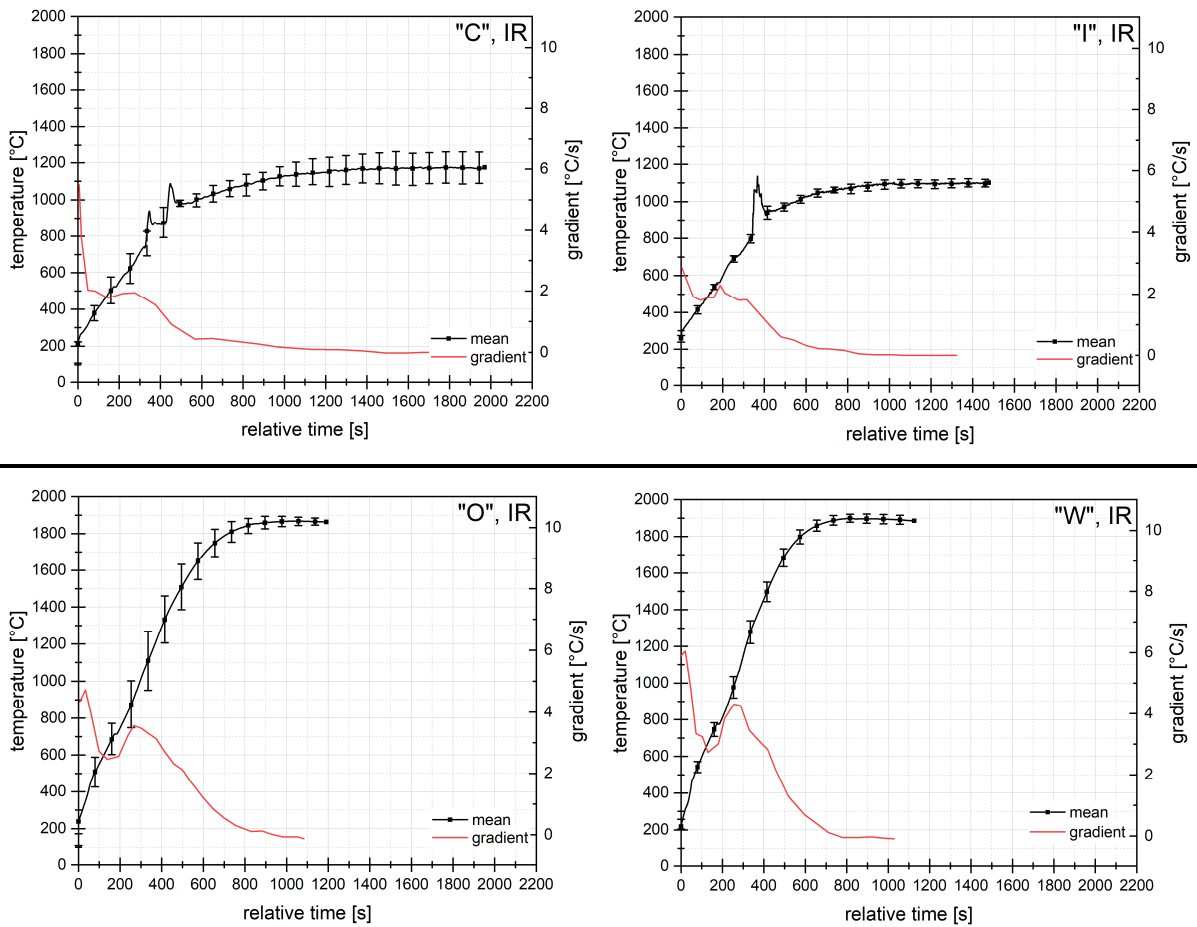


B. Temperature profiles

In the following subchapters the individual temperature curves of each sample for all four temperature measurement methods are shown.

Additionally, in **Table B-1** the gradients ($\Delta T/\Delta t$) of the mean temperature curves obtained by measurement with the IR camera can be seen.

Table B-1: Mean temperature curves of all four cases including standard deviation and the gradient ($\Delta T/\Delta t$), obtained by the infrared camera FLIR A615.

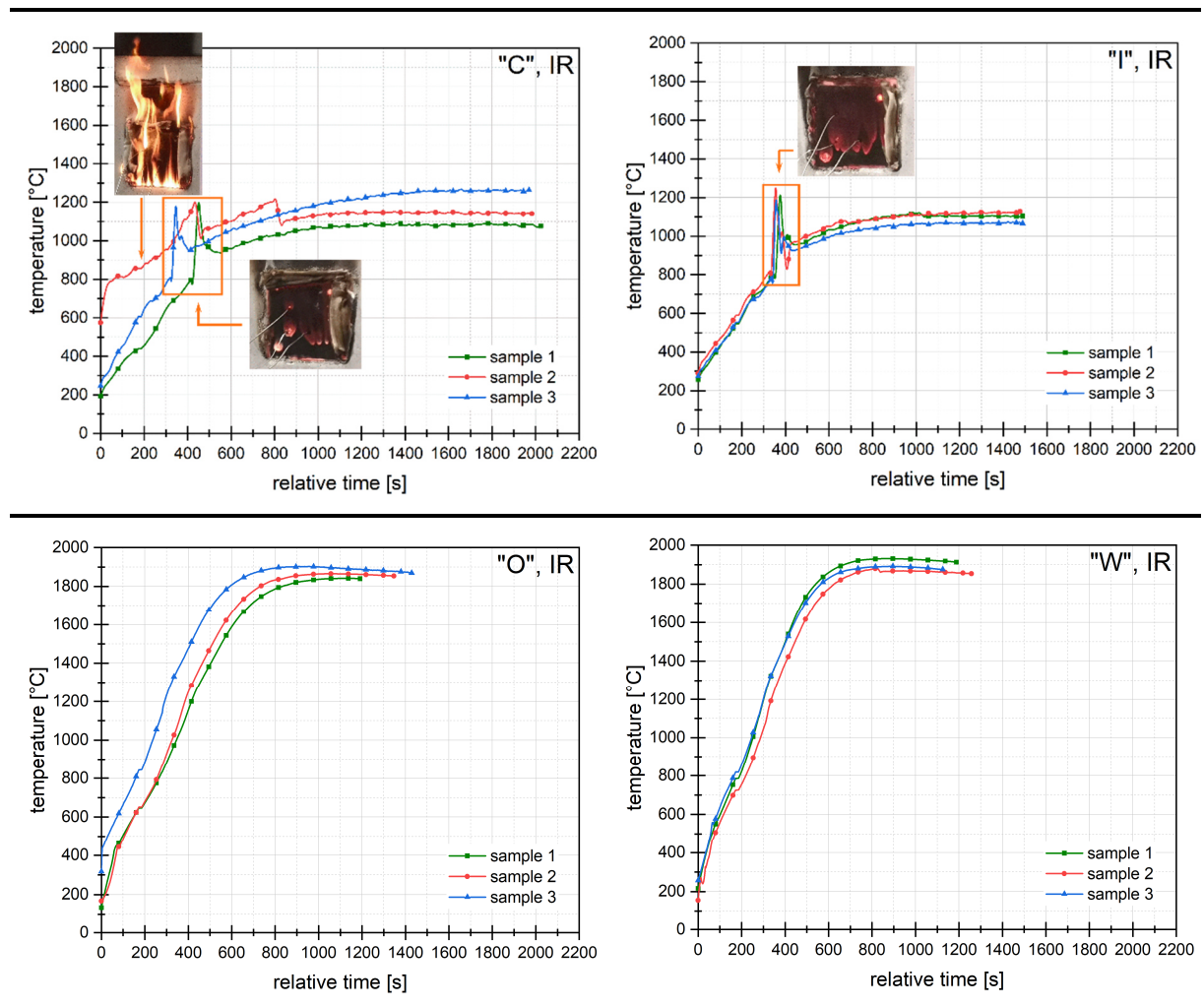


It is obvious, that in all four cases the gradient at the end of the measurement is around zero. This indicates that the temperature was constant when the measurement finished.

B.1 Infrared Camera

Table B-2 shows the temperature curves for the individual samples of the four different cases obtained by measurement with the IR camera.

Table B-2: Individual temperature curves of each sample for all cases, obtained by measurement with the IR camera



B.2 Pyrometer

In **Table B-3** the temperature curves for the individual samples of the four different cases obtained by measurement with the pyrometer can be seen.

Table B-3: Individual temperature curves of each sample for all cases, obtained by measurement with the pyrometer

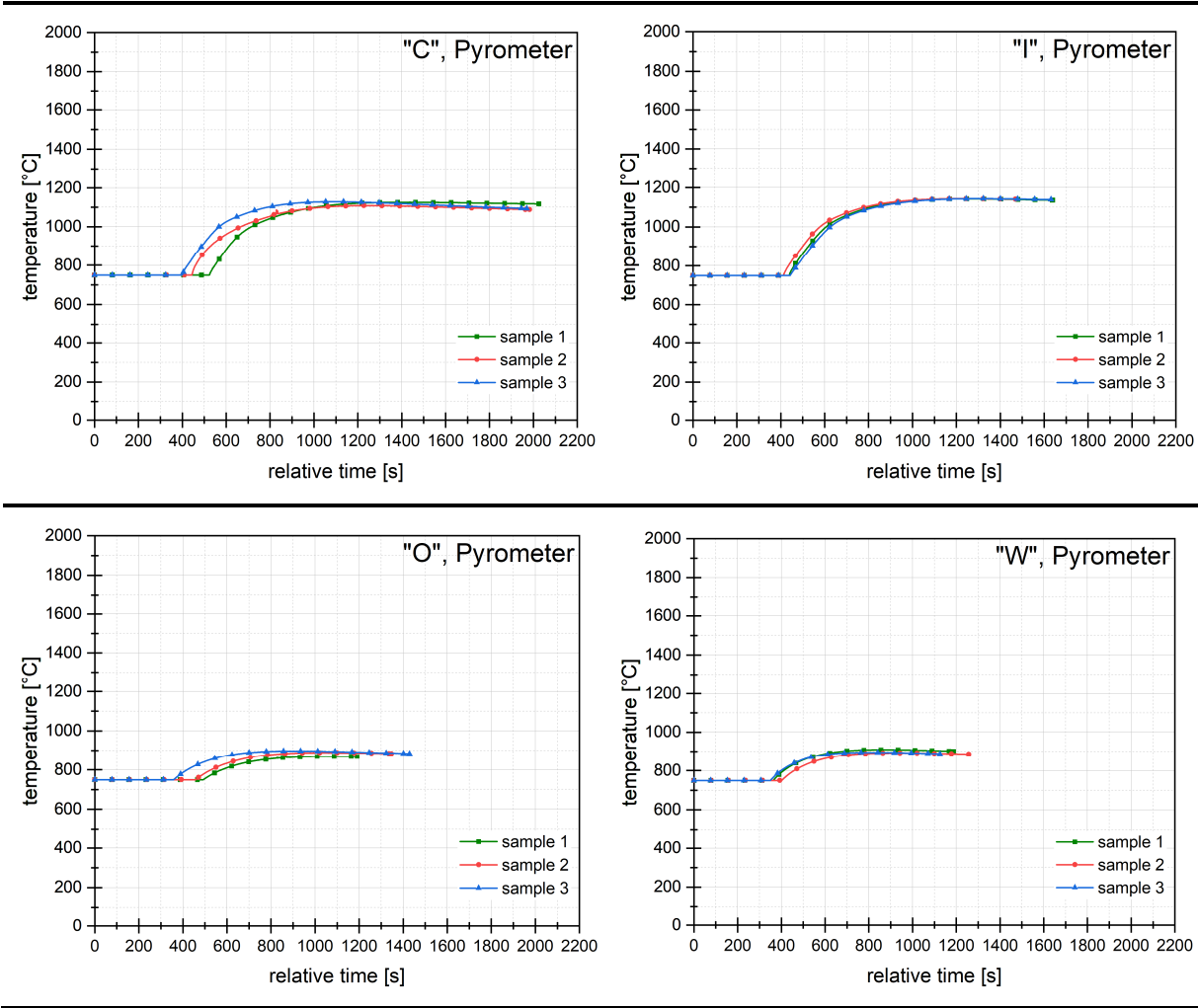


Figure B-1 shows the differences in the end temperatures of the mean temperature curves of each case in detail.

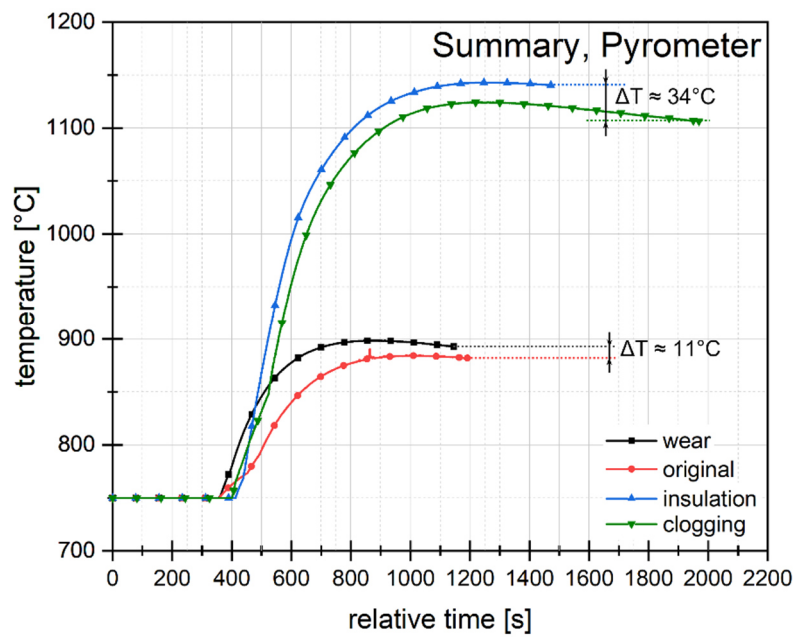


Figure B-1: Detailed diagram of the differences in the end temperatures of the mean temperature curves obtained by measurement with the pyrometer.

B.3 Thermocouples

The mean temperature curves which were placed in the middle and near the hot face of the samples can be seen in **Figure B-2** and **Figure B-3**.

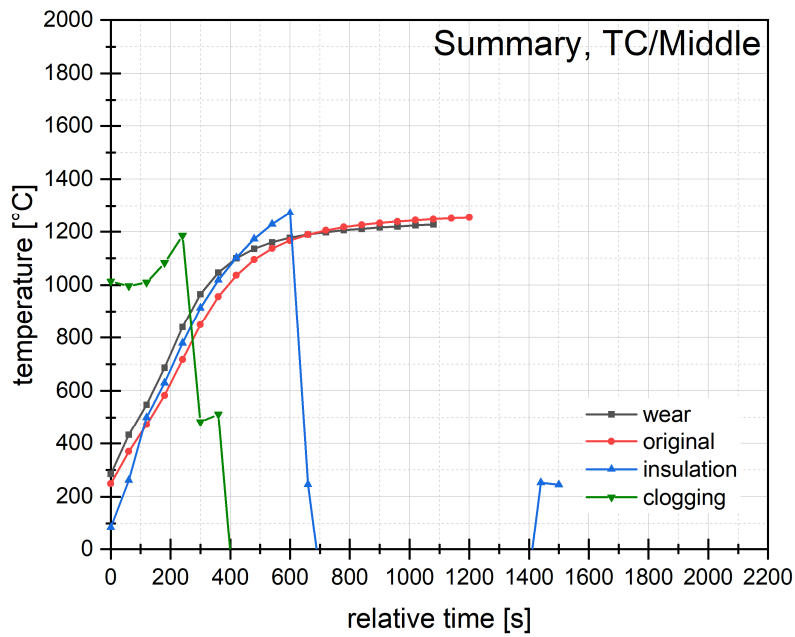


Figure B-2: Mean temperature curves obtained by thermocouples placed in the middle of the sample.

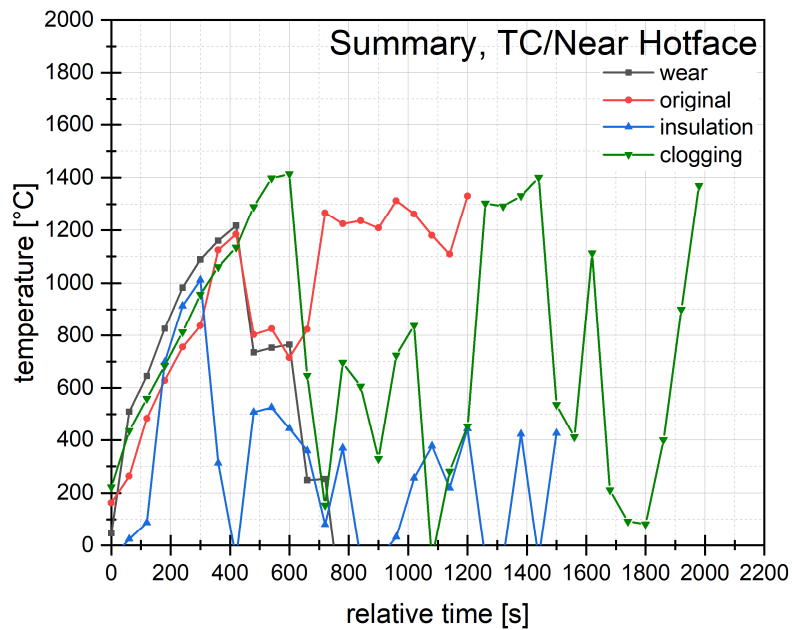
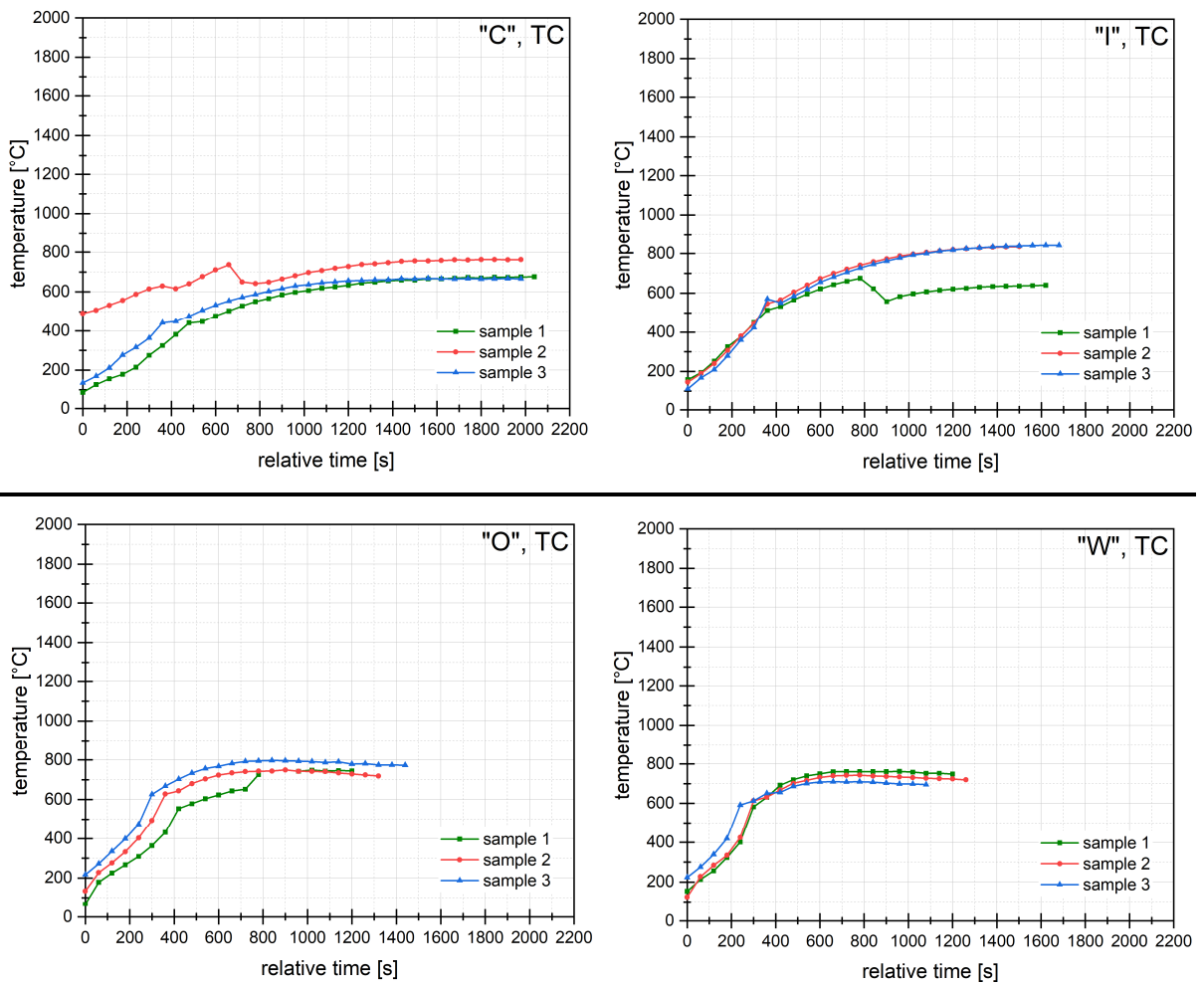


Figure B-3: Mean temperature curves obtained by thermocouples placed near the surface of the sample.

The temperature curves for the individual samples of the four different cases obtained by measurement with thermocouples on the surface can be seen in **Table B-4**.

Table B-4: Individual temperature curves of each sample for all cases, obtained by measurement with thermocouples placed on the surface.



In **Figure B-4** a detailed diagram of the mean temperature curves obtained by measurement with thermocouples can be seen.

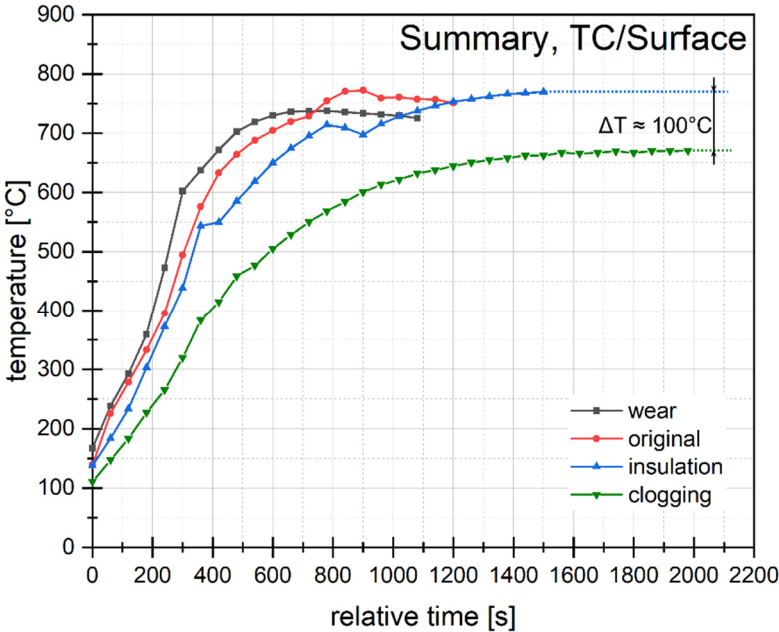


Figure B-4: Detailed diagram of the differences in the end temperatures of the mean temperature curves obtained by measurement with thermocouples.

PATRICIA POLATSCHEK

Peter Tunner-Straße 12 · 8700 Leoben



PERSÖNLICHE ANGABEN

Familienstand	ledig
Staatsangehörigkeit	Österreich
Geburtsdatum	25.02.1993
Geburtsort	Oberpullendorf

AUSBILDUNG

1999-2003	Volksschule Oberpullendorf
2003-2007	Bundesrealgymnasium Oberpullendorf
2007-2011	Bundesoberstufenrealgymnasium Oberpullendorf
2011-2020	Bachelor-Studium Metallurgie an der Montanuniversität Leoben
Seit 2020	Master-Studium Metallurgie an der Montanuniversität Leoben

BERUFSERFAHRUNG

seit Oktober 2015 geringfügige Beschäftigung bei RHI Magnesita GmbH